Emission of Energetic Neutral Atoms from Ganymede's Magnetosphere-Atmosphere Interaction

C. Michael Haynes[1], Sven Simon[1,2], Lucas Liuzzo[3]

[1]School of Earth and Atmospheric Sciences, Georgia Institute of Technology, Atlanta, Georgia, USA

[2]School of Physics, Georgia Institute of Technology, Atlanta, Georgia, USA

[3]Space Sciences Laboratory, University of California, Berkeley, California, USA

Key Points:

- We calculate the flux of energetic neutral atoms (ENAs) created by charge exchange between Ganymede's atmosphere and magnetospheric protons
- Reduced accessibility of Ganymede's closed field lines to Jovian protons causes local flux depletions in ENA images taken above the equator
- Pile-up of Jupiter's magnetospheric field above Ganymede's upstream hemisphere clearly depletes the ENA flux generated near the ramside apex

Corresponding author: C. Michael Haynes, `mhaynes@eas.gatech.edu`

Abstract

This study analyzes the emission of energetic neutral atoms (ENAs), generated by charge exchange between energetic protons and Ganymede's atmosphere. We also constrain the observability of such ENAs by an imaging instrument aboard a spacecraft. Our approach employs tracing tools that calculate the trajectories of magnetospheric parent protons near Ganymede. We determine the ENA flux through a hypothetical spherical detector encompassing the moon's atmosphere. We additionally generate synthetic ENA images, as seen by a point-like detector with a finite field of view. The complexity of Ganymede's electromagnetic environment is successively increased; we consider (i) uniform Jovian fields, (ii) the superposition of the moon's internal dipole with Jupiter's field, and (iii) draped fields from a hybrid model of Ganymede's plasma interaction. Our major results are: (a) In uniform fields, the ENA flux is elevated within a circular band on the detector sphere. Synthetic ENA images record a cluster of high flux near the moon's limb, with the position of this enhancement determined by the viewing geometry. (b) When including Ganymede's internal dipole, the flux through the sphere displays a localized increase above the ramside apex, mainly generated by protons on open field lines at mid-latitudes. In the synthetic images, the reduced ENA emissions from the closed field line region produce local flux depletions along the equator. (c) Pile-up of Jupiter's field significantly reduces the ENA flux from Ganymede's ramside atmosphere. (d) At energies above several keV, the emissions from Ganymede's atmosphere clearly exceed the ENA flux released from the moon's surface.

1 Introduction

Ganymede (radius $R_G = 2634.1\,\text{km}$) is a fully differentiated body (Anderson et al., 1996) and the largest planetary satellite in the solar system. Its nearly circular, prograde, and tidally locked orbit is located at a distance of $15R_J$ from Jupiter (radius $R_J = 71,492\,\text{km}$), approximately contained within the planet's equatorial plane. As such, Ganymede is permanently embedded within Jupiter's magnetosphere (Joy et al., 2002; Vogt et al., 2022). It is the only known moon to possess an internal dynamo process (Kivelson et al., 1996; Zhan & Schubert, 2012) which drives a global, intrinsic magnetic field, reaching an equatorial strength of $720\,\text{nT}$ (Kivelson et al., 2002; Jia et al., 2025). This internal field dominates the ambient Jovian magnetospheric field by up to an order of magnitude (e.g., Kivelson et al., 2004; Weber et al., 2022; Jia et al., 2025). Ganymede's in-

ternal field is largely dipolar (Saur et al., 2015; Weber et al., 2022) with a magnetic moment oriented nearly southward (Kivelson et al., 2002; Jia et al., 2025).

Due to the 9.6° offset between Jupiter's magnetic moment and spin axis, the component of the Jovian magnetospheric field parallel to Ganymede's orbital plane oscillates at the frequency of Jupiter's synodic rotation (e.g., Kivelson et al., 2002; Schilling et al., 2007). The periodic variation of this ambient field component induces a secondary magnetic field in Ganymede's conductive subsurface ocean (e.g., Seufert et al., 2011; Saur et al., 2015; Vance et al., 2021). However, this induction signal modifies the moon's net magnetic moment by less than 1% (e.g., Weber et al., 2022; Jia et al., 2025).

Ganymede has a dilute atmosphere that consists mainly of molecular oxygen (Hall et al., 1998; Marconi, 2007; Leblanc et al., 2023), molecular hydrogen (Barth et al., 1997; Alday et al., 2017), and a localized concentration of water vapor dominating the number density around the moon's subsolar apex (Roth et al., 2021). Elsewhere, molecular oxygen is the most dense constituent below about 200 km, with the extended corona of molecular hydrogen dominating at higher altitudes (e.g., Leblanc et al., 2017, 2023; Roth et al., 2025). This atmosphere is largely sourced from the water ice on Ganymede through sublimation and surface irradiation by magnetospheric ions and electrons (e.g., Johnson et al., 1981; Cooper et al., 2001; Marconi, 2007; Plainaki et al., 2015; Carnielli et al., 2020; Vorburger et al., 2022; Leblanc et al., 2023; Galli et al., 2025). Thus, dissociated products of water group molecules are also present in the atmosphere at low concentrations (e.g., H, O, and OH; see Turc et al., 2014; Allegrini et al., 2022). Ganymede's atmosphere is partially ionized by incident electrons and solar ultraviolet photons (e.g., Feldman et al., 2000; Carnielli et al., 2019; Carberry Mogan et al., 2023; Leblanc et al., 2023), generating an observable ionosphere (e.g., Kliore, 1998; Eviatar et al., 2001; Valek et al., 2022; Buccino et al., 2022).

Along Ganymede's orbit, the Jovian magnetosphere is populated by a dense, (sub)corotating thermal plasma (energies $E < 10\,\text{keV}$), largely originating from Io and transported radially outward (e.g., Southwood & Kivelson, 1987; Bagenal & Delamere, 2011; Bagenal et al., 2016; Kim et al., 2020; Devinat et al., 2024). This plasma overtakes Ganymede's Keplerian motion at speeds of $120-160\,\text{km/s}$ (Kivelson et al., 2004; Kim et al., 2020). The moon's internal field is strong enough to stand off the Jovian magnetospheric plasma and field above the surface, carving out a "mini-magnetosphere" in the ambient flow (e.g.,

Jia et al., 2008; Duling et al., 2014, 2022; Zhou et al., 2020; Stahl et al., 2023; Kivelson et al., 2025). Ganymede's environment represents an example of an open magnetosphere, where magnetic field lines are transported from the ramside toward downstream and then back upstream by means of the Dungey Cycle (Williams, 2001; Jia & Kivelson, 2021). In support of this picture, the Juno spacecraft found evidence of reconnection during its single close flyby of the moon: it detected both accelerated electrons upstream (Ebert et al., 2022) and the separatrix region of the reconnection site downstream (Joseph et al., 2024). Since the magnetosonic Mach number remains below unity at Ganymede (Kivelson et al., 2004; Jia & Kivelson, 2021), no bow shock is formed upstream of the moon. Instead, the deceleration and deflection of the impinging sub-Alfvénic plasma generate field line draping and an Alfvén wing system that connects to Jupiter's ionosphere through field-aligned currents (Neubauer, 1980; Gurnett et al., 1996; Bonfond et al., 2013; Hue et al., 2023). The Alfvén wing tubes are roughly cylindrical in shape, and their diameter perpendicular to the wing characteristics corresponds to the extent of the region dominated by the moon's atmosphere and internal magnetic field (Neubauer, 1998). The strength of the field perturbations from the plasma interaction oscillates with Ganymede's distance to the center of Jupiter's magnetospheric plasma sheet. This periodicity is caused by the dependence of the Jovian magnetospheric field strength and plasma density on the distance to the center of the planetary plasma sheet (Kivelson et al., 2004; Payan et al., 2015; Vogt et al., 2022; Santos et al., 2024; Kivelson et al., 2025).

Ganymede's mini-magnetosphere can be divided into regions with "open" and "closed" field lines (e.g., Paty & Winglee, 2004; Jia & Kivelson, 2021; Stahl et al., 2023). The region where magnetic field lines connect on both sides to the moon's surface (i.e., they are "closed") is located between latitudes of $\pm 30°$ in the orbital trailing hemisphere and $\pm 20°$ in the leading hemisphere (e.g., Jia et al., 2008; Stahl et al., 2023). Moving poleward from this region, the "open" magnetic field lines connect Ganymede's internal field to the Jovian magnetospheric field (Jia et al., 2008; Jia & Kivelson, 2021). The interface between these two regions is denoted the *open-closed field line boundary* (OCFB; see, e.g., Khurana et al., 2007). Furthermore, Jovian magnetospheric field lines (that do not connect to Ganymede at all) thread the moon's interaction region at high altitudes.

In addition to the thermal plasma, energetic ions and electrons (energies $E \gtrsim 10\,\mathrm{keV}$) constitute a second population of Jovian magnetospheric plasma to which Ganymede is continuously exposed (e.g., Williams et al., 1998; Mauk et al., 2004; Clark et al., 2019;

Paranicas et al., 2022). This population has been sampled near the moon by both the Galileo (e.g., Paranicas et al., 1999) and Juno (e.g., Clark et al., 2022) spacecraft. The energetic ion population consists mostly of protons, sulfur, and oxygen (e.g., Mauk et al., 2004; Clark et al., 2016). Energetic ions and electrons bounce between mirror points while drifting azimuthally through Jupiter's magnetosphere, impinging onto Ganymede's atmosphere and surface largely via open field lines connecting to the polar regions (Fatemi et al., 2016; Poppe et al., 2018; Liuzzo et al., 2020; Plainaki et al., 2022; Paranicas et al., 2022). A subset of these energetic particles may become trapped in the moon's mini-magnetosphere, forming radiation belts (Williams et al., 1997; Eviatar et al., 2000; Williams, 2001; Kollmann et al., 2022; Liuzzo et al., 2024). Irradiation of Ganymede's surface by such particles locally alters its brightness (e.g., Khurana et al., 2007; Liuzzo et al., 2020) and composition (e.g., Spencer et al., 1995; Calvin & Spencer, 1997). Precipitating ions and electrons also liberate neutral molecules from the surface via sputtering (e.g., Ip et al., 1997; Paranicas et al., 1999; Johnson et al., 2004). At Ganymede, the energies of sputtered neutrals cover several orders of magnitude. For a given incident ion energy, the flux of released neutrals decreases with increasing energy until reaching a species-dependent cutoff (e.g., Johnson, 1990; Johnson et al., 2004; Vorburger & Wurz, 2018).

Some of the particles sputtered from Ganymede's surface carry enough energy to escape the moon's local environment, traveling along nearly rectilinear trajectories. Such particles are classified as energetic neutral atoms (ENAs). Using the electromagnetic fields from a hybrid model (kinetic ions, fluid electrons), Poppe et al. (2018) calculated maps of the energy- and species-resolved magnetospheric ion fluxes incident onto Ganymede. Pontoni et al. (2022) then utilized these fluxes to compute the spatial distribution of sputtered ENA flux. These authors found that the ENA flux released poleward of the OCFB dominates that emanating from the low-latitude regions by several orders of magnitude for hydrogen and oxygen. Moreover, the model of Pontoni et al. (2022) revealed that particles sputtered from Ganymede's surface largely possess energies in the 10–100 eV range: averaged across the moon's surface, the sputtered ENA flux decreases by seven orders of magnitude when moving from 100 eV up to 100 keV. In addition to sputtered ENAs, some incident energetic ions may be backscattered from Ganymede's surface (e.g., Plainaki et al., 2010, 2012) and neutralized by electron capture in the process (Massey et al., 1970). Ion backscattering at Ganymede has been modeled by Szabo et al. (2024): again using the incident magnetospheric ion fluxes from Poppe et al. (2018), these authors found that

144 backscattered hydrogen and oxygen ENAs exceed those produced from sulfur by an or-

145 der of magnitude. By comparing their results for hydrogen ENAs to the sputtered fluxes

146 of Pontoni et al. (2022), the study of Szabo et al. (2024) demonstrates that backscat-

147 tering provides the dominant contribution to surface-generated hydrogen ENAs above

148 energies of 1 keV. Similar to the sputtered ENA flux, the flux of backscattered hydro-

149 gen decreases by six orders of magnitude moving from 100 eV to 100 keV. The models

150 of Pontoni et al. (2022) and Szabo et al. (2024) do not take into account any interactions

151 between the incident ions and Ganymede's neutral envelope. However, precipitating en-

152 ergetic ions may also undergo charge exchange with the atmosphere to produce ENAs.

153 The ENAs generated by this process may either exit the moon's interaction region or

154 impact its surface.

155   Observations of ENAs can be used by spacecraft detectors to construct "images"

156 of the interaction region. Examples of such ENA imagers are the Ion and Neutral Cam-

157 era (INCA; Mitchell et al., 1993; Krimigis et al., 2004) on Cassini, or the Jovian Ener-

158 getic Neutrals and Ions (JENI) instrument currently en route to Jupiter on the JUpiter

159 ICy moons Explorer (JUICE; Grasset et al., 2013; Tosi et al., 2024). The JENI detec-

160 tor can take images of hydrogen ENAs with energies ranging from 0.5–300 keV (Mitchell

161 et al., 2016; Galli et al., 2022). Hence, a large fraction of the backscattered and sput-

162 tered ENAs may not be energetic enough for detection by JENI (Pontoni et al., 2022;

163 Szabo et al., 2024), and would rather be observable by the low energy detector JNA (Jovian

164 Neutrals Analyzer; see Galli et al., 2022). Instead, we expect charge exchange in Ganymede's

165 atmosphere to be the dominant source for ENAs in this energy range (see also Haynes

166 et al., 2023; Haynes, Tippens, et al., 2025). In contrast to plasma or magnetometer ob-

167 servations which record information only along the one-dimensional spacecraft trajec-

168 tory, ENA imagers can provide two-dimensional context of Ganymede's plasma inter-

169 action by capturing the escaping ENA population as a whole. Since the emitted ENAs

170 stem from the motion of the Jovian energetic "parent ions" in Ganymede's vicinity, their

171 morphology is encoded with physical information about the moon's neutral envelope and

172 mini-magnetosphere (see also Tippens et al., 2022; Tippens, Roussos, et al., 2024; Tip-

173 pens, Simon, & Roussos, 2024; Haynes et al., 2023; Haynes, Tippens, et al., 2025). While

174 to date, no spacecraft has measured ENAs emanating from Ganymede's environment,

175 the JUICE mission is slated to perform multiple targeted flybys of the moon before ul-

176 timately going into orbit around it in late 2034 (Grasset et al., 2013). These close en-

counters will provide JENI a wide array of geometries from which ENA images of Ganymede's space environment may be captured. However, such ENA images require a template obtained by modeling to reconstruct the physics contained in the observed emission patterns.

In order to provide context for the upcoming JENI observations at Europa and Callisto, Haynes et al. (2023) modeled the global distribution of ENA flux from the atmospheres of both moons. These authors recorded the emissions emanating from Europa and Callisto through a (hypothetical) spherical detector that encloses each moon's entire atmosphere. Such a detector captures the entirety of the ENA emissions from a moon's atmosphere without truncation by, for instance, a limited field of view (FOV). They compared ENA flux maps obtained for uniform magnetospheric fields and draped fields from the AIKEF hybrid model (Müller et al., 2011). In addition, they considered different strengths of the plasma interaction, corresponding to different distances between the moons and the center of Jupiter's plasma sheet. Haynes et al. (2023) found that field line draping at Europa and Callisto diminishes the total ENA flux through the detector sphere and redistributes it across different longitudes. Despite that, the influence of draping only manifests in the global ENA emission morphology when each moon is near the center of Jupiter's plasma sheet where the perturbations to the electromagnetic fields are strongest.

The emission maps calculated by Haynes et al. (2023) do not emulate actual ENA images, thereby complicating any comparisons to spacecraft observations. Therefore, Haynes, Tippens, et al. (2025) built upon this effort by considering a realistic spacecraft detector geometry: such an instrument is point-like on the length scales of Europa's or Callisto's plasma interaction and has a limited FOV. Haynes, Tippens, et al. (2025) produced synthetic ENA images for six different viewing geometries, with the instrument's boresight vector pointing towards each moon's north or south pole, leading or trailing apex, and sub- or anti-Jovian apex. They showed that, e.g., the asymmetries in Europa's and Callisto's atmosphere are visible only in images taken north or south of each moon, exemplifying the strong dependence of ENA image morphology on the viewing direction. By generating synthetic ENA images for uniform and draped fields at both moons, Haynes, Tippens, et al. (2025) revealed that any non-uniformities in the fields are discernible in ENA images only for certain viewing geometries.

208 The strong internal field of Ganymede redistributes and deflects the energetic mag-
209 netospheric ions in a different way than the interaction with the ionospheres and weak
210 induced fields of Europa and Callisto (e.g., Poppe et al., 2018; Addison et al., 2021; Fatemi
211 et al., 2022; Liuzzo et al., 2022). Thus, previous modeling results for ENA emissions at
212 Europa and Callisto (Haynes et al., 2023; Haynes, Tippens, et al., 2025) are not imme-
213 diately applicable to constrain the ENA emissions expected from Ganymede's atmosphere.
214 Furthermore, since Ganymede's magnetosphere does not create a bow shock in the up-
215 stream plasma, context for the morphology of ENA emissions at Ganymede cannot be
216 directly adapted from our knowledge on ENA emissions at Earth (e.g., Roelof, 1987; Oga-
217 sawara et al., 2019; Brandt et al., 2022). In this study, we therefore seek to determine
218 the morphology of ENA emissions from Ganymede's atmosphere and its dependence on
219 the neutral envelope, the presence of the moon's internal field, and the interaction with
220 Jupiter's thermal magnetospheric plasma. We will investigate how each of these phys-
221 ical properties is observable by an ENA detector such as JENI. Our study is based upon
222 the same modeling framework that was recently used at Europa and Callisto: we apply
223 the global, spherical ENA detector model (Haynes et al., 2023) as well as the model for
224 a point-like spacecraft detector (Haynes, Tippens, et al., 2025) to study ENA emissions
225 from Ganymede's magnetosphere-atmosphere interaction. The remainder of the manuscript
226 is structured as follows: in section 2.1, we describe the AIKEF model which was used
227 to calculate the three-dimensional structure of the perturbed electromagnetic fields at
228 Ganymede. We briefly describe the models used to calculate the ENA flux through a de-
229 tector sphere around the moon's atmosphere and to generate synthetic ENA images in
230 sections 2.2 and 2.3, respectively. In section 3, we present our modeling results. We con-
231 clude with a brief summary of our major findings in section 4.

2 Modeling ENA Emissions from Ganymede's Atmosphere

233 In all models employed by this study, we use the Cartesian Ganymede Interaction
234 System (GPhiO), originating at the moon's center with the coordinates $\mathbf{r} = (x, y, z)$.
235 The GPhiO system has the following normalized basis vectors: $\hat{\mathbf{x}}$ is aligned with the coro-
236 tational flow direction, $\hat{\mathbf{z}}$ is parallel to the Jovian spin axis, and $\hat{\mathbf{y}} = \hat{\mathbf{z}} \times \hat{\mathbf{x}}$ bears roughly
237 toward Jupiter. The model also makes use of the West longitude system. The north and
238 south poles are located at latitudes of $\pm 90°$. Along the equator, a longitude of $0°$ W in-

dicates the Jupiter-averted apex, 270° W corresponds to the upstream apex, and longitude decreases moving westward (clockwise) around the moon.

2.1 Model of Ganymede's Electromagnetic Environment

In order to describe the three-dimensional structure of the electromagnetic fields near Ganymede, we apply existing output from the AIKEF hybrid model (Müller et al., 2011). The hybrid approach treats the electrons as a massless and charge-neutralizing fluid, while the thermal ions are represented by individual particles. In this way, the model is able to simultaneously capture the vastly different dynamics of Jovian magnetospheric ions and pick-up ions from Ganymede's ionosphere, the gyroradii of which can differ by over an order of magnitude (e.g., Paty et al., 2008). We use the electromagnetic fields obtained by Stahl et al. (2023) for the conditions during Juno's close flyby of Ganymede on its PJ34 orbit in 2021. This flyby occurred when the moon was near the center of the Jovian magnetospheric plasma sheet (Weber et al., 2022) where the impinging thermal plasma is most dense (Bagenal & Delamere, 2011). Hence, the draping and pile-up of Jupiter's magnetic field near the moon are more pronounced than at larger distances to the center of the sheet. However, due to Ganymede's strong internal field, the variability in the plasma interaction with distance to the sheet is much weaker than at, e.g., Europa or Callisto (Duling et al., 2014; Jia & Kivelson, 2021; Fatemi et al., 2022; Haynes et al., 2023). Therefore, the structure of the moon's interaction region during the Juno flyby can be considered qualitatively representative of its environment across an entire synodic rotation of Jupiter. For this reason, our study includes only the upstream conditions observed during the PJ34 flyby, and we will investigate the variability in ENA emissions with Ganymede's distance to the center of Jupiter's plasma sheet in a future effort. Here, we provide a brief overview of the parameters used by Stahl et al. (2023) to generate the electromagnetic field output used in our ENA models. For more details, we refer the reader to the discussion of the parameter set labeled "Setup V" in Stahl et al. (2023).

The Juno flyby occurred with the subsolar apex located at $(-0.67,\, 0.74,\, 0.00)\, R_G$ on Ganymede's surface (Hansen et al., 2022). The AIKEF runs of Stahl et al. (2023) include a single, composite upstream ion species with an average mass of 14 amu (near the mass of O^+) and charge $+e$ to represent the makeup of the Jovian plasma sheet at Ganymede's orbit (e.g., Kivelson et al., 2004; Jia et al., 2010; Duling et al., 2022; Romanelli et al.,

2022). The model of Stahl et al. (2023) employs an upstream number density of $n_0 = 10\,\text{cm}^{-3}$, consistent with Juno measurements outside the mini-magnetosphere (Allegrini et al., 2022; Kurth et al., 2022). The bulk velocity of the sub-Alfvénic thermal plasma flow is set to $\mathbf{u}_0 = (130, 0, 0)\,\text{km/s}$, within the range of observed velocities at Ganymede's orbit (Kivelson et al., 2004; Jia & Kivelson, 2021).

A spatially uniform Jovian magnetospheric field $\mathbf{B}_0 = (-15, 24, -75)\,\text{nT}$ with magnitude $|\mathbf{B}_0| = 80.2\,\text{nT}$ is included in AIKEF, obtained from Juno magnetometer data by linearly interpolating (about closest approach) the field vectors observed inbound and outbound of the mini-magnetosphere (Duling et al., 2022; Stahl et al., 2023). In the unperturbed Jovian plasma outside of the moon's interaction region, the electric field is given by $\mathbf{E}_0 = -\mathbf{u}_0 \times \mathbf{B}_0$. Ganymede's permanent dipole field is described by the magnetic moment $\mathbf{M}_\text{d} = (-4.1, 9.0, -131.0) \times 10^{27}\,\text{J/nT}$, extracted from analysis of Galileo and Juno magnetometer observations (Kivelson et al., 2002; Weber et al., 2022; Jia et al., 2025). To account for the finite conductivity of Ganymede's subsurface ocean, the induced magnetic moment $\mathbf{M}_\text{ind}$ is assumed to be $\alpha = 84\%$ the inductive response of a perfect conductor (see also Kivelson et al., 2002). A recent modeling effort refined this estimate to $\alpha = 72\%$ by subtracting the contributions of plasma currents from the analyzed magnetic field signatures, using MHD simulations (Jia et al., 2025). The permanent moment $\mathbf{M}_\text{d}$ and induced moment $\mathbf{M}_\text{ind}$ are superimposed to obtain Ganymede's net intrinsic moment $\mathbf{M}_\text{int}$. Between the two values of α, the net moment $\mathbf{M}_\text{int}$ only differs by 0.7% in magnitude and 0.1° in orientation (see also Jia et al., 2025). Hence, the value of $\alpha = 84\%$ used by Stahl et al. (2023) is more than adequate to reproduce key features of Ganymede's plasma interaction.

In AIKEF, Ganymede's atmosphere is assumed to consist of O_2, H_2, and H_2O. For O_2 and H_2, Stahl et al. (2023) included spherically symmetric density profiles, described by barometric laws. The surface densities used for these species read $n_{O_2} = 6.0 \cdot 10^{13}\,\text{m}^{-3}$ and $n_{H_2} = 7.5 \cdot 10^{12}\,\text{m}^{-3}$, with scale heights given by $h_{O_2} = 250\,\text{km}$ and $h_{H_2} = 1{,}000\,\text{km}$, respectively. The density profile of H_2O takes into account the accumulation of this species around Ganymede's subsolar point, as observed by Roth et al. (2021). The drop in H_2O number density with altitude is still barometric, but the density peaks at the subsolar apex ($n_{H_2O} = 2.2 \cdot 10^{14}\,\text{m}^{-3}$) and decreases moving angularly away from it. The scale height of this component reads $h_{H_2O} = 200\,\text{km}$. In the model, Ganymede's ionosphere is generated by electron impacts and photoionization. Stahl et al. (2023) demonstrated

that the atmosphere and ionosphere models used in AIKEF are suitable to quantitatively reproduce the timeseries of ionospheric O_2^+ and H_2^+ densities observed along the Juno flyby trajectory. Their approach can also replicate the general shape and magnitude as well as fine structures in the observed magnetic perturbations. Overall, Ganymede's ionosphere was found to have only a minor influence on the electromagnetic signatures of the interaction (Stahl et al., 2023). Asymmetries in the density profiles of atmospheric O_2 and H_2 have been proposed by several modeling efforts (e.g., Leblanc et al., 2017; Plainaki et al., 2020; Vorburger et al., 2024). However, the possible presence of such asymmetries has not yet been reconciled with magnetometer and plasma observations from the Juno and Galileo flybys of Ganymede: all currently available models of the moon's plasma interaction treat the density profiles of oxygen and hydrogen as spherically symmetric (e.g., Paty et al., 2008; Jia et al., 2009; Duling et al., 2014, 2022; Romanelli et al., 2022). Constraining the contribution of asymmetries in the O_2 and H_2 envelopes to Ganymede's electromagnetic environment is beyond the scope of our current work. Instead, we apply the results obtained with the atmosphere representation used in Stahl et al. (2023).

The spatial domain we consider in this study is a cube with sides extending $-8R_G \leq x \leq 12R_G$, $|y| \leq 10R_G$, and $|z| \leq 10R_G$. A hierarchical Cartesian grid is used, with the highest resolution of $0.027R_G$ achieved near Ganymede, thereby resolving the scale heights of all three atmospheric species (Stahl et al., 2023).

2.2 Modeling the Global ENA Emission Pattern at Ganymede

We utilize the model of Haynes et al. (2023) in order to calculate the ENA flux from Ganymede's atmosphere through a spherical detector encapsulating the moon and its neutral envelope. We generate maps of the ENA flux recorded by this detector for three distinct field configurations, successively increasing in complexity:

(i) perfectly uniform electromagnetic fields ($\mathbf{B}_0$, $\mathbf{E}_0$) in the vicinity of Ganymede. This setup accounts for the Jovian field $\mathbf{B}_0$, but it does *not* include Ganymede's internal magnetic moment $\mathbf{M}_{\mathrm{int}}$.

(ii) the superposition of the Jovian magnetospheric field and Ganymede's internal field (described by $\mathbf{M}_{\mathrm{int}}$), yielding a spatially non-uniform magnetic field $\mathbf{B}$. The electric field is given by $\mathbf{E} = -\mathbf{u}_0 \times \mathbf{B}$ (analogous to, e.g., Liuzzo et al., 2019).

(iii) draped electromagnetic fields, obtained from the AIKEF hybrid model for the Juno flyby (Stahl et al., 2023).

This approach allows us to first isolate the role of Ganymede's internal field in shaping the ENA emissions. The second step (i.e., moving from case (ii) to case (iii)) provides constraints on the contributions of plasma effects.

The model of Haynes et al. (2023) traces energetic Jovian parent ion macroparticles through Ganymede's electromagnetic environment. Some of these ions enter the moon's atmosphere, undergo charge exchange with the neutral gas, and produce ENAs. We refrain from providing further details on the operation of this model, as it is described in detail in our preceding publication. In the following, we only enumerate the parameters that are chosen specific to Ganymede's environment.

Analogous to our studies of Europa and Callisto, the model considers ENA production from charge exchange with magnetospheric protons (mass m_p). At Ganymede's two neighboring moons, the intensity of ENA emissions recorded by the detector sphere is highest between parent ion energies of $10-100\,\text{keV}$ (Haynes et al., 2023). Consistent with this result, we study ENA production in Ganymede's atmosphere for the energy range from $E_L = 10\,\text{keV}$ to $E_U = 100\,\text{keV}$. Proton gyroradii vary from $r_{g,L} = 180\,\text{km} \approx 0.07 R_G$ to $r_{g,U} = 570\,\text{km} \approx 0.22 R_G$ across this regime, that is, from less than the smallest atmospheric scale height in our model ($h_{\text{H}_2\text{O}}$) to more than double it. We do not include the contributions of energetic oxygen or sulfur ions to ENA generation in Ganymede's atmosphere. At the moon's orbit, these two species can be singly or multiply charged. However, only singly charged ions can undergo charge exchange on the small length scales of Ganymede's interaction region (see also Nénon & André, 2019). Due to uncertainty in the distribution of charge states for oxygen and sulfur (Clark et al., 2016, 2020), it is not clear which fraction of each ion population would actually contribute to atmospheric ENA generation. Furthermore, published data for the charge exchange cross sections between, e.g., magnetospheric O^+ and atmospheric O_2 only partially cover our energy range (Lindsay & Stebbings, 2005; Loand & Tite, 1969). Further discussion on our decision to consider only ENAs generated by protons is provided by Haynes et al. (2023) and Haynes, Tippens, et al. (2025).

The domain of the global ENA model is again a cube of side length $20 R_G$ (see section 2.1), the faces of which are aligned with the coordinate planes of the GPhiO sys-

tem. Placing a launch grid on all six sides of Ganymede accounts for the portion of the energetic proton population that does not travel along the corotation direction, but instead approaches the moon with a large velocity component along the Jovian magnetic field lines (see Haynes et al., 2023, for details). The large extent of the model domain ensures that ions crossing its outer faces cannot re-enter Ganymede's atmosphere through sheer gyration. The faces of the particle tracing domain are covered with regularly spaced nodes. From each node, parent proton macroparticles of a given initial energy $E \in [E_L, E_U]$ are launched such that their velocities uniformly populate a spherical surface in velocity space with radius $\sqrt{2E/m_p}$. Since the gyroradii of the parent protons differ by more than a factor of 3 between the lower and upper edges of our considered energy range, the dynamics of parent protons and their ENA production vary substantially between energies of E_L and E_U. Thus, analogous to our approach for Europa and Callisto, we initialize monoenergetic proton populations with energies of $E \in \{10, 40, 70, 100\}$ keV. A spacing of $\Delta x = \Delta y = \Delta z = 0.15 R_G$ is used between adjacent nodes on the Cartesian launch grid. At each node, neighboring initial velocity vectors for the parent protons are separated by $\Delta \theta_v = \Delta \phi_v = 15°$ in latitude or longitude.

Analogous to Haynes et al. (2023), each H^+ macroparticle is initialized with a differential flux J sampled from an energetic ion spectrum $I(E)$ that was observed outside of Ganymede's mini-magnetosphere. We employ the energetic proton spectrum $I(E)$ recorded during Juno's crossing of Ganymede's orbit in 2019 while the spacecraft was located at a large (longitudinal) distance from the moon (Figure 4 in Paranicas et al., 2021). This spectrum includes intensities $I(E)$ between 10 eV and 50 keV from the Jovian Auroral Distributions Experiment (JADE; McComas et al., 2017; Allegrini et al., 2020) and measurements between 50 keV and 5 MeV from the Juno Energetic particle Detector Instrument (JEDI; Mauk et al., 2017). Hence, this dataset for $I(E)$ covers the entire energy range $[E_L, E_U]$ where we investigate ENA generation. While the energetic proton spectrum procured by JEDI during the PJ34 flyby is also available in the literature (Paranicas et al., 2022), the published data from that event are restricted to energies above 50 keV. That is, it only partially covers the energy range $[E_L, E_U]$ where significant ENA production from the atmosphere is expected. Thus, we proceed with the energetic proton spectrum of Paranicas et al. (2021) to represent the ambient Jovian environment near Ganymede through the entire interval $[E_L, E_U]$. At any given energy E above 50 keV (where both Paranicas et al. (2021) and Paranicas et al. (2022) provide data), the intensities from

these two spectra differ by less than 30%. Hence, the morphology and intensity of recorded ENA fluxes using $I(E)$ from Paranicas et al. (2021) are expected to only slightly deviate from the respective values calculated with the spectrum of Paranicas et al. (2022). We emphasize that the goal of our study is to gain general understanding of the ENA emission morphology at Ganymede, but not to reproduce specific ENA observations from a spacecraft (since such data do not yet exist).

Using observations from JADE and JEDI, Sarkango et al. (2023) showed that the pitch angle distribution (PAD) of Jovian magnetospheric protons outside of Ganymede's mini-magnetosphere is slightly anisotropic; proton fluxes at field-aligned pitch angles are up to a factor of 2 higher than at pitch angles near 90° (see their Figure 1). However, our present model treats the ambient PAD as uniform. Due to the large number of cases already under consideration, the contribution of anisotropies in the PAD will be constrained in a subsequent study. We note that at Europa, including a similar degree of anisotropy in the PAD was found to leave the strength and morphology of the ENA flux through the detector mostly unchanged, compared to a uniform PAD (see section 3.3 in Haynes et al., 2023). Still, because of its strong internal field, this result does not immediately translate to Ganymede.

The motion of energetic H^+ macroparticles is traced through the electromagnetic fields for setups (i), (ii) or (iii) with a Runge-Kutta integrator of fourth order accuracy. This tool uses an adaptive timestep of $T_g/160$ within Ganymede's atmosphere and $T_g/80$ outside of it, where T_g is the ion's *local* gyroperiod (see also Tippens et al., 2022; Haynes et al., 2023). In principle, proton trajectories can be scattered by, for instance, electron cyclotron waves and Whistler waves, which have been observed in the vicinity of Ganymede by Galileo (Shprits et al., 2018) and Juno (Kurth et al., 2022). However, we follow the approach of Haynes et al. (2023) and Haynes, Tippens, et al. (2025) and do not take into account the influence of local interactions between protons and plasma waves. This effect may be analyzed in a subsequent study, using a time-dependent model for the electromagnetic environment. Such an effort would also require the three-dimensional distribution of these waves near Ganymede to be known.

In order to ensure consistency with the draped fields from AIKEF, it is imperative that the composition and density profile of Ganymede's atmosphere in the ENA model match those used in the hybrid model. The atmosphere is treated as a continuum, and

each parent ion generates an ENA macroparticle of weight $|\mathrm{d}J|$ during every timestep within the neutral envelope. The ENA intensity $|\mathrm{d}J|$ produced along a certain path element is calculated from

$$\mathrm{d}J = -\sum_i \sigma_i n_{n,i} J \mathrm{d}s \qquad , \tag{1}$$

where the index i ranges over all three neutral species: $i \in \{\mathrm{O_2}, \mathrm{H_2}, \mathrm{H_2O}\}$. The parameter σ_i represents the charge exchange cross section between protons and atmospheric species i, the quantity $n_{n,i}$ is the local number density of neutral species i, and $\mathrm{d}s$ is the path length covered by the parent proton during the respective timestep. This ENA adopts the momentary velocity of its parent proton. The cross sections for charge exchange between energetic protons and atmospheric $\mathrm{O_2}$ or $\mathrm{H_2O}$ are taken from Lindsay and Stebbings (2005) and Wedlund et al. (2019), respectively; see also Figure 2 of Haynes et al. (2023). For the energy range considered, the charge exchange cross section between protons and $\mathrm{H_2}$ is provided by Tawara et al. (1985). The outer boundary of the atmosphere in our model is located at $|\mathbf{r}| = 3R_G$, below which more than 99.5% of the neutral gas for each species is contained. The detector sphere is also placed at this radial position, thereby encompassing the region of substantial ENA production. For ENAs traveling away from Ganymede, the flux that they carry to the point of intersection with the detector is recorded and binned. The spherical detector captures all ENAs crossing its pixels, not only those propagating radially. ENAs hitting the surface do not contribute to the flux through the detector sphere. However, by tracking the locations of their impacts on Ganymede, the model immediately delivers maps of the ENA flux from the moon's atmosphere onto its surface. Results from this model are discussed in section 3.1.

2.3 Generating Synthetic ENA Images at Ganymede

We use the model presented by Tippens, Roussos, et al. (2024) and Haynes, Tippens, et al. (2025) to produce synthetic images of the ENAs emanating from Ganymede's atmosphere. This model accounts for the limited field of view (FOV) of a realistic ENA detector as well as its point-like extent compared to the length scales of Ganymede's minimagnetosphere. To avoid calculating the motion of parent ions that never enter the moon's neutral envelope, these ions are launched along the detector's lines of sight and then traced *backward* in time. The model detector is represented by a portion of a spherical surface, divided into small angular segments (i.e., pixels) in azimuth and elevation. Since the FOV and angular resolution of JENI are not yet available in the peer-reviewed literature, we

463 adopt the approach of Haynes, Tippens, et al. (2025) and use parameters representative

464 of Cassini's INCA instrument (Krimigis et al., 2004): the detector surface in our model

465 spans 90° in azimuth and 120° in elevation (Mitchell et al., 2005). Similar to Haynes,

466 Tippens, et al. (2025), this FOV is discretized into pixels extending 1° in both azimuth

467 and elevation.

468   Every pixel on the model detector is the footpoint of an individual line of sight (LOS)

469 that extends radially outward. If a LOS intersects Ganymede's atmosphere, the section

470 of the LOS within the neutral envelope is discretized into segments of length $\Delta\ell = 0.015 R_G \approx$

471 40 km. We again employ the same description of Ganymede's atmosphere as in AIKEF

472 (see also section 2.2). Thus, the resolution $\Delta\ell$ is about 1/5 the smallest atmospheric scale

473 height in our model and can comfortably resolve radial changes in the neutral density.

474 As in the global ENA model, we consider only ENA generation by Jovian magnetospheric

475 protons. Akin to the approach of Haynes, Tippens, et al. (2025), the energy range for

476 the atomic hydrogen channel of our model detector overlaps with both the energies cap-

477 tured by JENI ($0.5\,\text{keV} \leq E \leq 300\,\text{keV}$) and the energies where the observable ENA

478 flux from the atmosphere is expected to be most intense. We select a similar energy range

479 for our channel as in the global model (see section 2.2) and the study of Haynes, Tip-

480 pens, et al. (2025), namely from 10 keV to 70 keV. Over this (hypothetical) energy chan-

481 nel, the gyroradii of protons vary from $180\,\text{km} \approx 0.07 R_G$ to $477\,\text{km} \approx 0.18 R_G$. In or-

482 der to resolve the differences in proton dynamics across these energies, we discretize this

483 interval in steps of 10 keV; i.e., we consider seven discrete energies. From every segment

484 on a LOS, an energetic parent proton is initialized at each of these seven energies and

485 traced backwards in time. Every proton is backtraced until it encounters one of two fates.

486 A backtraced proton that reaches the ambient Jovian environment far from Ganymede

487 by crossing the walls of the model domain can emit ENAs into the detector along the

488 LOS from which it was launched. Alternatively, a backtraced proton that impacts Ganymede's

489 surface cannot contribute to the synthetic ENA image. Analogous to section 2.2, the do-

490 main where energetic proton trajectories are calculated is again a cube of side length $20 R_G$.

491   In principle, a backtraced parent proton can exit Ganymede's local environment

492 along a Jovian magnetospheric field line, mirror at high planetary latitudes, and return

493 to impact the moon's surface. However, in the energy window we consider, the drift dis-

494 placements of such protons along the corotational direction $\hat{\mathbf{x}}$ are substantially larger than

495 the extent of Ganymede's interaction region (Poppe et al., 2018; Kollmann et al., 2022).

Hence, once a backtraced proton reaches an outer face of the model domain, it can be safely concluded that it contributes to the ENA flux along the LOS from which it was launched. Since protons at the energies considered typically remain trapped in Ganymede's internal field for no more than one drift orbit around the moon (Poppe et al., 2018), all backtraced trajectories will ultimately either reach the ambient Jovian magnetospheric environment (i.e., contribute to the ENA image) or intersect the surface (i.e., deliver no ENA flux to the image).

Once a backtraced proton reaches the ambient Jovian environment, it is assigned a differential flux J by sampling the energetic proton spectrum of Paranicas et al. (2021), as also used in the global ENA model (see section 2.2). When generating synthetic ENA images, the Jovian magnetospheric proton PAD near Ganymede is again treated as isotropic. Any parent proton that contributes to the image is subsequently traced through the atmosphere with a positive timestep as it performs charge exchange with the neutral gas in a manner analogous to the global ENA model (see section 2.2 in Haynes et al., 2023). However, in contrast to the global model where all ENAs traveling away from Ganymede are recorded by the detector sphere, only the single ENA macroparticle emitted along the LOS (in the final timestep of the forward-tracing procedure) contributes to the synthetic image. The ENA flux recorded by each pixel of the model detector is obtained by summing the contributions of individual ENAs over all parent ion energies and LOS segments.

To facilitate comparison between our synthetic and (future) observed ENA images, two steps are carried out after collecting the ENA flux into each pixel. First, the resolution of the synthetic image is downscaled to match the 32×32 pixel grid of INCA (Krimigis et al., 2004). The process of using a higher resolution and subsequently downscaling emulates the behavior of the pixels on an actual detector, which can still receive ENAs with velocity vectors that are slightly inclined against their boresight vectors (Tippens, Roussos, et al., 2024). While the angular width of the pixels on JENI is expected to be smaller than on INCA (Mitchell et al., 2016), our preceding results for Europa and Callisto strongly suggest that using a reduced pixel size would not introduce any novel morphological features to the synthetic images (Haynes, Tippens, et al., 2025). Second, a point spread function (PSF; Dialynas et al., 2013) is applied to the synthetic ENA images in order to account for the slight scattering of the incoming ENA flux by the instrument foils (Krimigis et al., 2004; Mitchell et al., 2016). As described extensively by Tippens, Roussos, et al.

(2024) and Haynes, Tippens, et al. (2025), the choice of timestep Δt for the model scales the overall brightness of the synthetic ENA images. By choosing the *same* timestep of $|\Delta t| = T_g/500$ everywhere within the model domain, we ensure that the morphology (i.e., the *relative* brightness of different features in the image) is adequately predicted. However, we caution the reader that the *absolute* flux values from our synthetic ENA images cannot be immediately compared to future JENI observations.

For each configuration of the electromagnetic fields (i.e., setups (i), (ii), and (iii)), several synthetic ENA images are generated for different viewing geometries of the detector. In each image, the detector's boresight bears radially inward (towards the moon's center). For all synthetic ENA images, the detector is positioned at $|\mathbf{r}| = 4R_G$, which is larger than the radius of the global spherical detector ($|\mathbf{r}| = 3R_G$; see section 2.2). In this way, the detector is able to capture emissions from the entirety of Ganymede's atmosphere in our model, providing straightforward access to the physics shaping the images. While JUICE will capture ENA images from $4R_G$ altitude (Boutonnet et al., 2024), the spacecraft will also reach altitudes as low as a few hundred kilometers. ENA images taken at such altitudes will contain emissions from only a limited portion of the atmosphere, making it far more challenging to identify, for instance, the role of field line draping or the internal dipole. Therefore, we defer this case to a follow-up study. The viewing geometries used to capture synthetic ENA images are the same as those employed by Haynes, Tippens, et al. (2025): we consider detectors above Ganymede's north and south poles $(0, 0, \pm 4R_G)$, above the sub-Jovian and anti-Jovian apices $(0, \pm 4R_G, 0)$, as well as above the wakeside and ramside apices $(\pm 4R_G, 0, 0)$. The results are discussed in section 3.3.

3 Results and Discussion

3.1 The Global Distribution of Detectable ENA Emissions from Ganymede's Atmosphere

Figure 1 depicts maps of the ENA emissions recorded on a spherical detector surrounding Ganymede's atmosphere. The model results for cases (i), (ii), and (iii) are arranged into the left, center, and right columns, respectively. Each row corresponds to a distinct initial proton energy, that is, $10\,\text{keV}$, $40\,\text{keV}$, $70\,\text{keV}$, and $100\,\text{keV}$ moving from top to bottom. The ENA flux captured by the detector is projected onto a flat surface
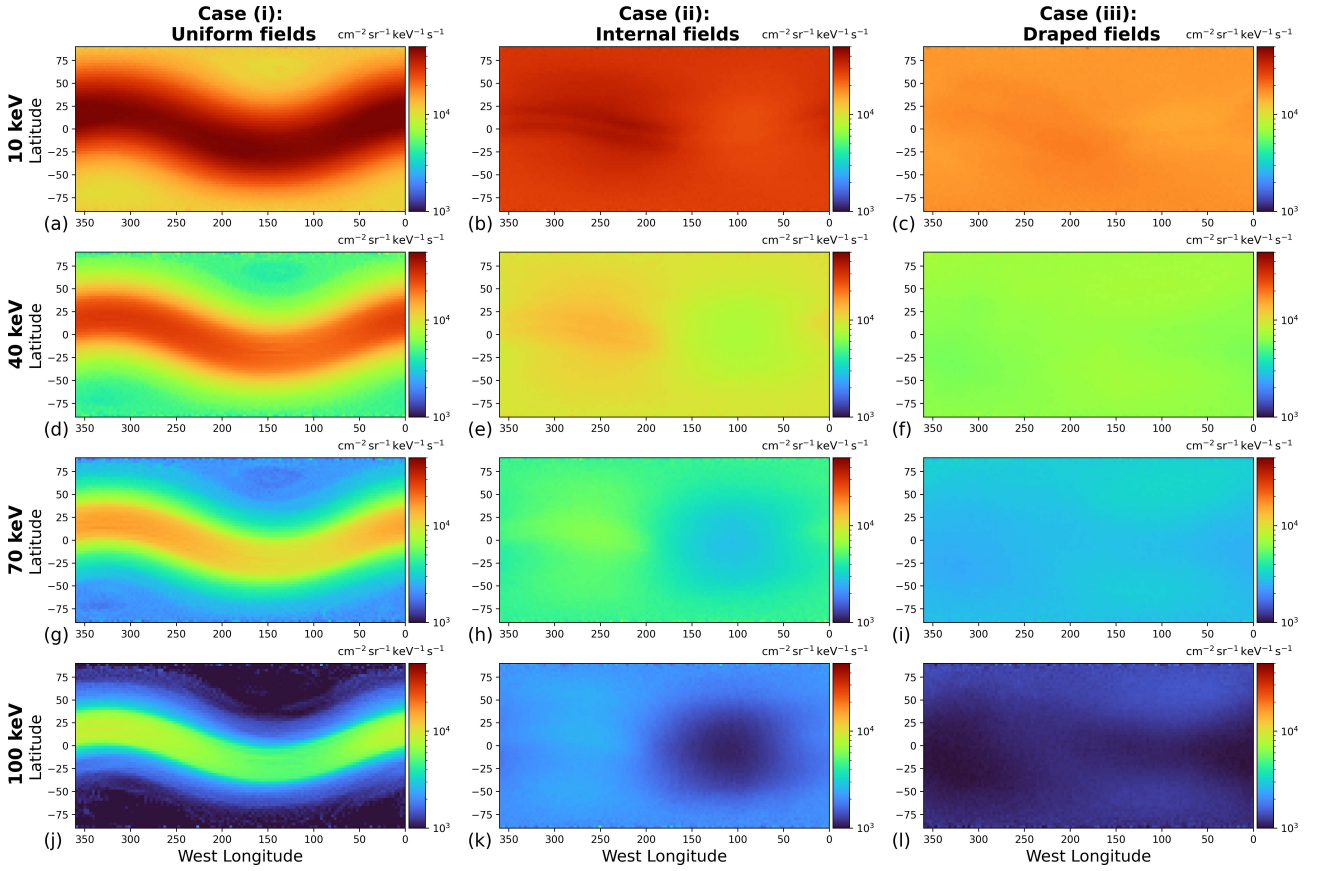
Figure 1. Global maps of energetic neutral atom (ENA) fluxes from Ganymede's atmosphere through a concentric spherical detector of radius $3R_G$, for the conditions during the Juno PJ34 flyby (see Stahl et al., 2023). The maps are projected onto a rectangular surface using the West Longitude system. The columns each show the modeled ENA flux for a certain field configuration (see section 2.2): uniform Jovian magnetospheric fields (case (i)) in the left column (panels (a), (d), (g), and (j)), the superposition of uniform Jovian fields and Ganymede's internal fields (induced and permanent, case (ii)) in the center column (panels (b), (e), (h), and (k)), and draped electromagnetic fields from AIKEF (case (iii)) in the right column (panels (c), (f), (i), and (l)). The rows correspond to different energies for the parent protons when initialized on the starting grid: 10 keV in row (a-c), 40 keV in row (d-f), 70 keV in row (g-i), and 100 keV in row (j-l). In all panels, the colorscale is logarithmic and ranges from $1 \cdot 10^3 \, [\mathrm{cm^2 \, sr \, keV \, s}]^{-1}$ to $5 \cdot 10^4 \, [\mathrm{cm^2 \, sr \, keV \, s}]^{-1}$.

using the West Longitude coordinate system. The logarithmic colorscale used in Figure 1 is the *same* for all panels.

562   The absolute values of the ENA flux recorded on the spherical detector drop by

563 around an order of magnitude between the lowest and highest initial parent proton en-

564 ergies (shown in the top and bottom rows of Figure 1). The flux values at lower ener-

565 gies are concentrated around the upper end of the colorscale (red/orange), and those at

566 higher energies are clustered at the low end (blue/green), with saturation at both ex-

567 tremes. In consequence, any fine structures in the ENA emission morphology are diffi-

568 cult to discern within the individual panels. To facilitate the identification of such sig-

569 natures, Figure 2 shows the *same* flux maps as Figure 1; however, each row in Figure

570 2 has a narrowed colorscale that only spans a factor of 10 in ENA flux. When moving

571 from low to high energies in Figure 2, the values within the covered flux range succes-

572 sively decrease.
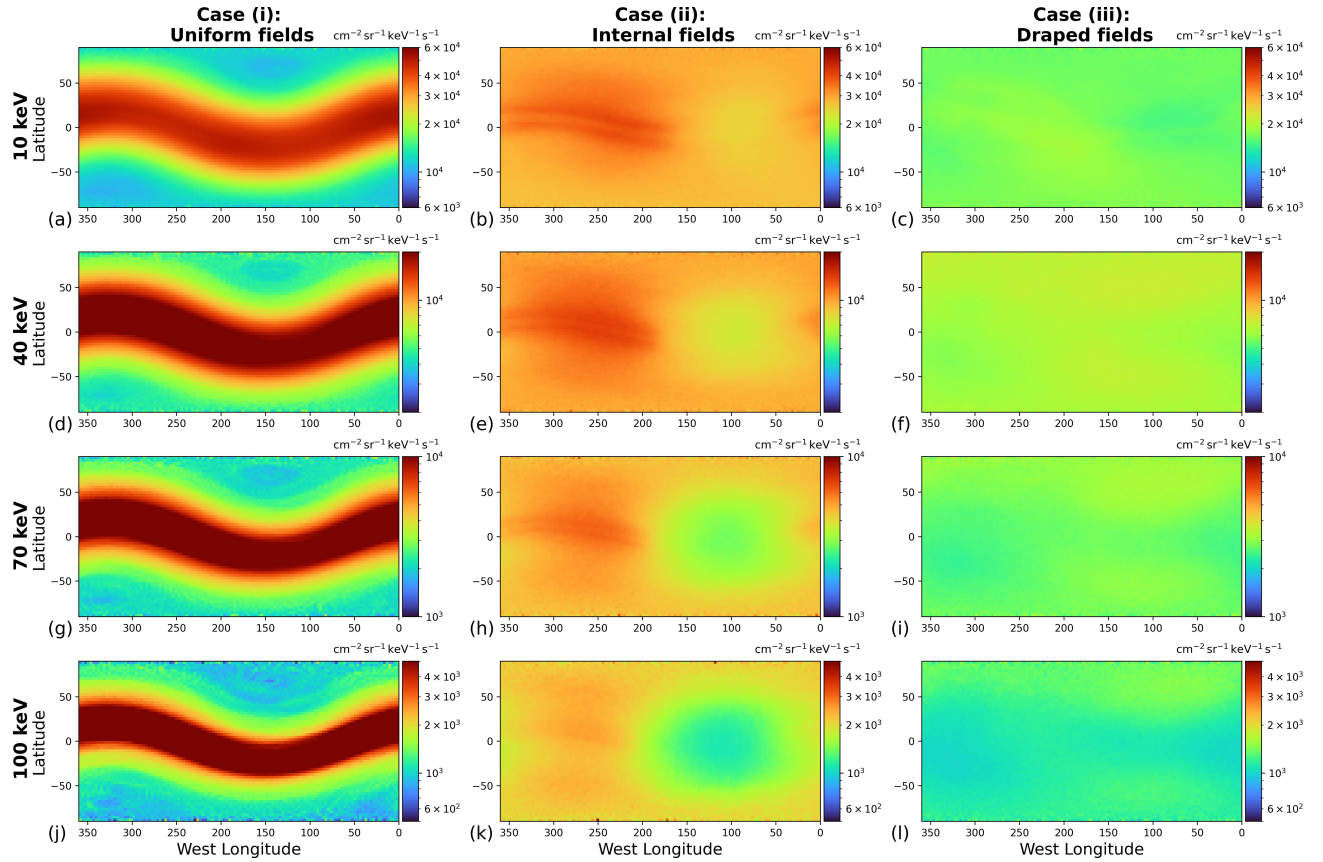
Figure 2.   Global maps of ENA flux emanating from Ganymede's atmosphere, identical to those displayed in Figure 1, but with a *different* range of the colorscale in each row to reveal fine structures in the emission morphology. The figure is organized in the same manner as Figure 1. The colorscale is logarithmic, with its range changing from row to row. The minimum and maximum values in each row are always one order of magnitude apart.

573　　　　In uniform Jovian magnetospheric fields (case (i)), the ENA emissions recorded on

574　the detector exhibit a similar morphology at all initial parent proton energies (panels (a),

575　(d), (g), and (j) of Figures 1 and 2): a band of elevated ENA flux wraps around the en-

576　tire detector, present at all longitudes and at slightly varying latitudes. In the projected

577　flux maps, the band displays an apparent "waviness". This morphology strongly resem-

578　bles the ENA emission patterns found for the (hypothetical) case of perfectly uniform

579　magnetospheric fields at Europa (Haynes et al., 2023). At the time of the Juno flyby, the

580　Jovian magnetospheric field at Ganymede's orbit was inclined against the $(-z)$ axis by

581　approximately $20.7°$. In one of the configurations considered at Europa (see their sec-

582　tion 3.2), the ambient Jovian field is tilted against the $(-z)$ axis by a similar value of

583　$28.5°$. Due to the similarities between the field geometries and ENA flux patterns at Ganymede

584　and Europa, we provide only a brief explanation of the physical mechanism responsible

585　for the band's formation, and we refer the reader to Haynes et al. (2023) for more de-

586　tails.

587　　　　The band of elevated ENA flux is largely produced by parent protons with pitch

588　angles of $\alpha \approx 90°$. Such protons possess a weak translational velocity along the Jovian

589　magnetic field $\mathbf{B}_0$. In the energy range considered, proton gyroradii at Ganymede are

590　similar to or smaller than the atmospheric scale heights (see section 2.2). Hence, due to

591　their ability to gyrate many times within the moon's atmosphere, the path length through

592　the neutral envelope is maximized for parent protons with $\alpha \approx 90°$. ENAs emitted by

593　such parent protons mainly travel within planes that intersect Ganymede's atmosphere

594　perpendicular to the ambient field. Therefore, these emissions form a circular band of

595　elevated ENA flux on the detector.

596　　　　Due to the tilt of $\mathbf{B}_0$ against the north-south axis, the band of elevated ENA flux

597　is not parallel to the detector's equator: inspection of, for instance, Figure 2(g) reveals

598　a $20°$ variation in the latitude of the band's top or bottom edge across different West

599　Longitudes. The inclination of the Jovian magnetospheric field against the north-south

600　direction results in a corresponding tilt of the parent proton gyroplanes against the $z =$

601　0 plane. This yields an identical rotation of the band's orientation on the detector sphere,

602　causing the apparent "waviness" in the maps of Figures 1 and 2. In other words, the wavi-

603　ness stems from the chosen projection in these figures. The latitudinal thickness of the

604　band can be estimated by comparing the radius of the detector sphere to the largest at-

605　mospheric scale height, namely that of H_2. Evaluating equation (21) of Haynes et al. (2023)

for a detector of radius $3R_G$ and a scale height of $1,000\,\mathrm{km}$ yields a latitudinal thickness of $54.8°$, consistent with the latitudinal extent of the band in the left columns of Figures 1 and 2.

The overall drop in ENA fluxes with increasing energy, visible in every column of Figure 1, is also similar to the behavior identified at Europa and Callisto (Haynes et al., 2023). Both the cross sections for charge exchange with all three atmospheric species (Tawara et al., 1985; Lindsay & Stebbings, 2005; Wedlund et al., 2019) and the energetic proton intensity $I(E)$ in the ambient Jovian plasma (Paranicas et al., 2021) diminish with increasing proton energy. When moving from $10\,\mathrm{keV}$ up to $100\,\mathrm{keV}$, the cross sections fall by roughly an order of magnitude, whereas the ambient proton fluxes decrease by a factor of 2. The decrease of these two quantities lowers the likelihood of charge exchange interactions between protons and Ganymede's neutral gas; thus the ENA flux recorded on the spherical detector falls with increasing proton energy. Since the decrease in the cross sections clearly exceeds that of the proton fluxes, this effect is mainly driven by the lower cross sections.

The results obtained for a superposition of Ganymede's internal field with the ambient Jovian field $\mathbf{B}_0$ (case (ii)) reveal a significantly modified ENA emission morphology. Comparing the left and center columns of Figure 1 or 2 indicates that the intensity of the ENA fluxes in case (ii) varies substantially less with longitude and latitude on the detector than in uniform fields (case (i)). For instance, at an initial proton energy of $40\,\mathrm{keV}$, the intensity of the detectable ENA flux in uniform fields differs by over an order of magnitude between the center of the band feature and the detector's polar caps (Figures 1(d) and 2(d)). In contrast, the difference between minimum and maximum intensities in the flux maps (at the same initial energy) is only a factor of 2 when Ganymede's internal field is included (Figures 1(e) and 2(e)). The band feature largely disappears, and the ENA flux directed towards the poles is elevated compared to case (i). The low-latitude region, where Ganymede's internal field dominates proton dynamics, extends to altitudes of approximately $1\,R_G$ (e.g., Jia & Kivelson, 2021). In the dilute atmosphere beyond this region, the probability for charge exchange drops and only limited ENA production occurs: even the largest atmospheric scale height (that of H_2) is only $1,000\,\mathrm{km} \approx 0.38R_G$. Thus, Ganymede's internal field reduces the protons' ability to penetrate into the low-latitude atmosphere, inhibiting the production of the band feature from case (i). The moon's internal field also modifies their trajectories in the po-

lar regions, thereby causing the adjustments to the ENA flux patterns at high latitudes between the left and center columns of Figure 1.

When Ganymede's internal field is included (case (ii)), the ENA flux recorded on the downstream, equatorial portion of the detector (longitudes of $60°-130°$ W) is depleted by 30% to 40% compared to its surroundings; see, e.g., the green region in Figure 2(h). This reduction in ENA flux is driven by a diminished accessibility of the low-latitude, wakeside atmosphere to incident Jovian protons. Due to the roughly parallel orientation of the Jovian field $\mathbf{B}_0$ and Ganymede's dipole $\mathbf{M}_{\text{net}}$, the dominant contribution of ENA flux at equatorial detector latitudes stems from parent protons with pitch angles around $90°$. Those with steeper pitch angles mostly emit ENAs towards higher latitudes on the detector (see also Haynes et al., 2023). Energetic Jovian magnetospheric protons with pitch angles near $90°$ mainly gain access to the atmosphere around Ganymede's downstream apex by gyrating onto a closed field line and completing a partial drift orbit around the moon (Poppe et al., 2018). As shown with a combination of hybrid modeling for the fields and energetic ion tracing, protons in the considered energy range are capable of completing partial drift orbits (Poppe et al., 2018). However, protons on such orbits may be removed from Ganymede's mini-magnetosphere by impacting the moon's surface or by gyrating back onto an adjacent open field line (Williams, 2001; Kollmann et al., 2022). Thus, only a certain fraction of these protons ultimately reach the downstream region (Cooper et al., 2001) and generate detectable ENAs, causing the wakeside depletion in flux (Figures 1 and 2). As illustrated by the second column of Figure 2, the downstream reduction in recorded ENA flux becomes more widespread as proton energy increases. Since gyroradii grow with energy, protons with higher energies are more prone to impacting the surface or exiting the closed field line region via gyration. Hence, the downstream reduction of detected ENA flux becomes more pronounced at higher initial proton energies.

As can be seen in the center column of Figures 1 and 2, a localized region of enhanced ENA flux is recorded on the upstream, equatorial portion of the detector (between longitudes of $200°-300°$ W). Aside from the wakeside depletion, this is the only significant morphological feature in the flux maps for case (ii). The ENA fluxes recorded within this "patch" are elevated from their surroundings on the detector by 30%–60%. Overlain on the patch, two roughly parallel "stripes" of enhanced ENA flux are visible (see, e.g., red segments in Figure 2(b)). The patch feature and its sub-structure take a
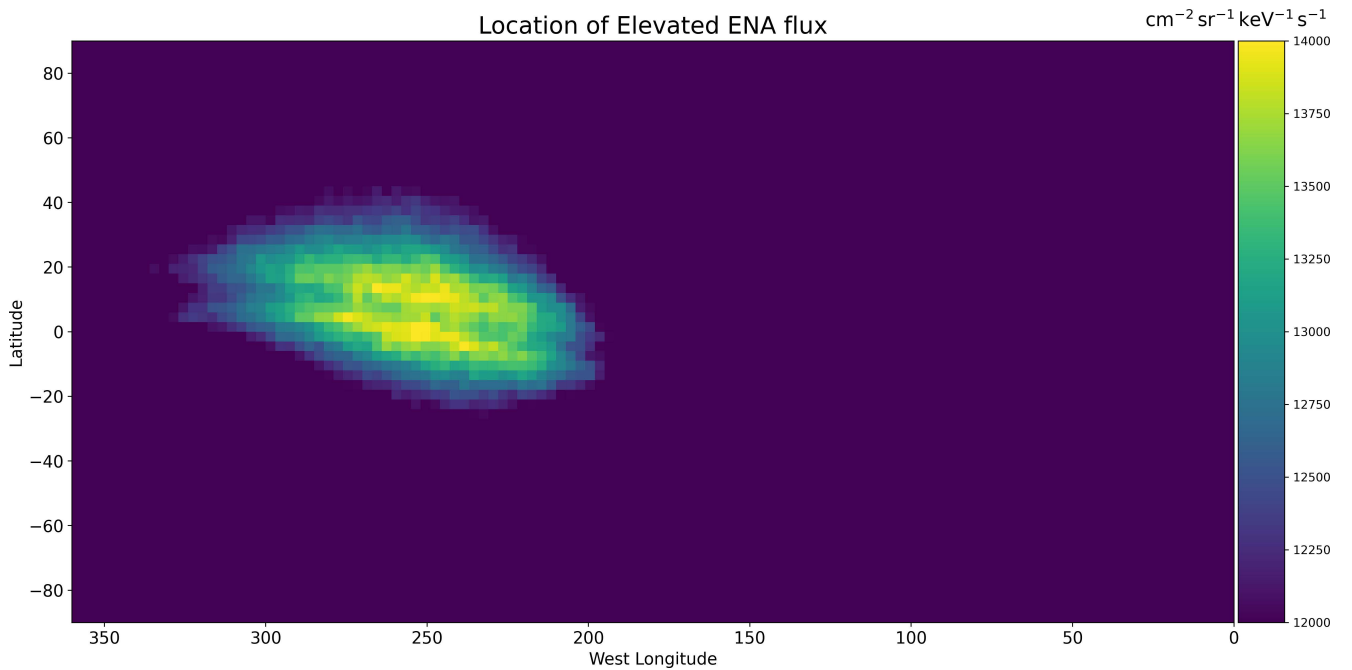
Figure 3. ENA flux recorded on the spherical detector for a superposition of Ganymede's internal field and the Jovian magnetospheric field (case (ii)) and at an initial parent proton energy of $40\,\mathrm{keV}$. The vertical and horizontal axes represent latitude and West Longitude, respectively. This flux map is identical to those shown in Figures 1(e) and 2(e). However, a *linear* colorscale is used, with its lower edge chosen to facilitate the identification of a "patch" of elevated ENA flux in the emission pattern on the detector. For this purpose, pixels with ENA fluxes below $12,000\,[\mathrm{cm}^2\,\mathrm{sr}\,\mathrm{keV}\,\mathrm{s}]^{-1}$ (the minimum value on this scale) appear purple. Fluxes above this threshold define the feature under investigation and appear in yellow, green, and blue. Only locations on the detector with fluxes above $12,000\,[\mathrm{cm}^2\,\mathrm{sr}\,\mathrm{keV}\,\mathrm{s}]^{-1}$ are included in our subsequent analysis of the associated parent proton population.

similar form at all initial proton energies. However, comparison of the results between $10\,\mathrm{keV}$ and $100\,\mathrm{keV}$ indicates that the "stripes" become less prominent with increasing energy.

In order to uncover the physical mechanism driving this enhancement, we first aim to identify the parent proton population that contributes ENA flux to this feature on the detector. We expect the mechanism forming the patch to be similar at all initial proton energies, so we focus our analysis on an initial energy of $40\,\mathrm{keV}$. Figure 3 depicts the ENA flux into the patch (at $E = 40\,\mathrm{keV}$), isolated from the adjacent emissions recorded

680 on the detector. That is, the flux map in Figure 3 is identical to those in Figures 1(e)

681 and 2(e). However, the colorscale in Figure 3 is linear, and locations on the detector with

682 ENA fluxes greater than $12,000 \, [\mathrm{cm^2 \, sr \, keV \, s}]^{-1}$ mark the extent of the patch feature (light

683 blue, green, yellow). Conversely, locations appear purple when the recorded ENA fluxes

684 are below this threshold. The ENAs generating the flux pattern on the detector are emit-

685 ted along straight line tangents to the momentary velocities of the parent protons. Hence,

686 with knowledge of the detector pixels that comprise the patch, we can identify the po-

687 sitions of parent protons when they contribute ENA flux to the feature.

688   Using the locations of the parent protons contributing to the emission feature in

689 Figure 3, we construct a histogram of the ENA flux *produced* by these protons as a func-

690 tion of altitude (Figure 4(a)). That is, the ENA flux into the patch, generated within

691 a certain altitude range, is summed over all parent proton contributions $|\mathrm{d}J|$, irrespec-

692 tive of their latitude and longitude at the instant of ENA generation. The *generated* and

693 *detected* ENA fluxes differ: in general, the ENA flux produced within a specific range

694 of altitudes "spreads out" to be recorded at different longitudes and latitudes on the de-

695 tector. The altitude distribution of generated ENA flux (cyan) for the 40 keV proton pop-

696 ulation contributing to the patch feature is displayed in Figure 4(a). The generated ENA

697 flux is sorted into horizontal bins of $R_G/26 \approx 101 \, \mathrm{km}$.

698   Even though the density of Ganymede's atmosphere is maximized at the surface,

699 the production of detectable ENA emissions drops precipitously at low altitudes (cyan

700 line in Figure 4(a)). Furthermore, approximately 80% of the ENA flux emitted towards

701 the patch on the detector is generated within $1 R_G$ of the moon (vertical red line). The

702 cyan curve indicates that maximal ENA production takes place between altitudes of ap-

703 proximately $1,000$–$1,100 \, \mathrm{km}$ ($\approx 0.4 R_G$). The peak at intermediate altitudes is the re-

704 sult of two competing trends. First, the atmospheric density at Ganymede decreases rapidly

705 with increasing distance to the surface: compared to their values at the surface, the H_2

706 and O_2 densities have fallen by approximately one and four orders of magnitude at an

707 altitude of $1 R_G$, respectively. At higher altitudes, the neutral gas is too dilute to facil-

708 itate substantial ENA production, despite the intensities J of the proton macroparticles

709 being largely unattenuated near the top of the atmosphere. Second, traveling deeper into

710 the atmosphere, the intensity J of the flux carried by the proton macroparticles is con-

711 tinuously depleted through charge exchange interactions with the neutral gas in consec-

712 utive timesteps. Thus, when reaching low altitudes, an increasingly larger fraction of the
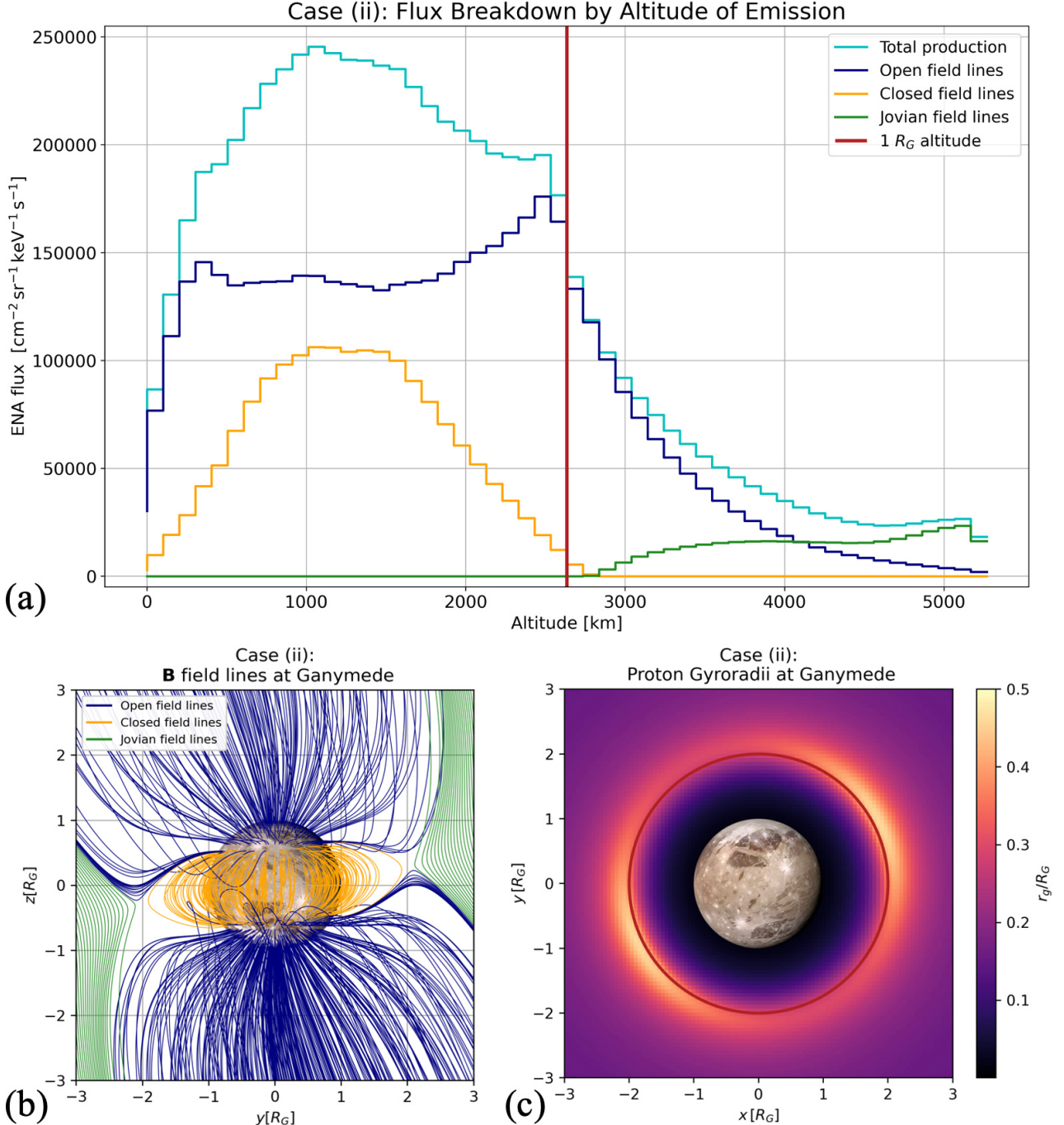
Figure 4. Relation between ENA emissions and the magnetic field topology near Ganymede. For case (ii), panel (a) provides an altitude profile of the generation region for the ENA flux emitted toward the "patch" feature identified in Figure 3. The histogram is computed by grouping the ENA flux generated by the contributing 40 keV protons into altitude bins of approximately 100 km height, irrespective of the longitude and latitude of ENA production. The horizontal axis displays the altitude above Ganymede's surface, and the vertical axis represents the locally produced ENA flux. Panel (a) takes into account the points of origin for all ENAs contributing to the patch feature. The total ENA production within each altitude bin is shown in cyan. The plot also identifies the ENA populations emanating from protons on "closed" field lines that connect to Ganymede at both ends (orange curve), "open" field lines that connect Ganymede's internal field to Jupiter's field (navy curve), and Jovian magnetospheric field lines which do not connect to the moon (green curve). The vertical red bar corresponds to an altitude of $1 R_G$. It is emphasized that panel (a) does *not* show the locations where ENA flux is being recorded. Panel (b) illustrates the magnetic field topology near Ganymede for case (ii). Field lines are depicted in the $x = 0$ plane, i.e., in a cut perpendicular to the incident flow $\mathbf{u}_0$. The field lines are colored analogous to panel (a): open field lines are navy, closed field lines are orange, and Jovian field lines are green. Also for case (ii), panel (c) depicts a map of the local 40 keV proton gyroradii near Ganymede in the equatorial ($z = 0$) plane. A pitch angle of $\alpha = 90°$ was assumed to generate this plot. The colorscale ranges from $r_g = 0$ to $r_g = 0.5 R_G \approx 1,317$ km. The dark red circle corresponds to an altitude of $1 R_G$.

713   parent proton population has already been attenuated by ENA production and can no

714   longer contribute to the patch feature. These two counteracting processes result in the

715   majority of ENA production taking place at intermediate altitudes, as suggested by the

716   cyan curve in Figure 4(a). This mechanism is somewhat analogous to the formation of

717   an ionospheric production maximum at a certain altitude above a planet's surface: the

718   intensity of the ionizing UV radiation increases with growing distance to the surface, whereas

719   the atmospheric neutral density decreases.

720   An illustration of the magnetic field lines near Ganymede for case (ii) is depicted

721   in Figure 4(b). Open field lines (navy) connect to Ganymede in the polar regions, whereas

722   closed field lines (orange) are located near the magnetic equator and connect to the moon's

723   surface on both sides. Jovian magnetospheric field lines (green) do not connect to Ganymede

724   at all, but may still thread the moon's atmosphere at high altitudes. When emitting ENAs

725   toward the patch feature in Figure 3, parent protons may be situated on field lines that

726   fall into any of these three categories. We decompose the proton population contribut-

727   ing to the patch (cyan line in Figure 4(a)) based on the type of field line upon which they

728   are located at the instant of ENA emission. A proton macroparticle emits many ENAs

729   while inside Ganymede's atmosphere (section 2.2 and Haynes et al., 2023), and the po-

730   sition of the parent proton is considered at the instant of each ENA emission. In other

731   words, the *same* proton macroparticle may generate ENAs on, e.g., open *and* closed field

732   lines at *different* points in time, and both contributions to the patch are counted sep-

733   arately at their respective locations.

734   We determine the type of field line at the instantaneous location of the proton, not

735   the guiding center. For this reason, uncertainty in the classification procedure stems from,

736   e.g., protons momentarily located on a closed field line, but with their guiding centers

737   attached to an adjacent open or Jovian field line. This can occur, for instance, near the

738   OCFB at mid-latitudes, or in the separatrix region where open, closed, and Jovian field

739   lines accumulate (Figure 4(b)). The impact of this uncertainty is determined by the size

740   of proton gyroradii near the moon. Figure 4(c) depicts the gyroradii r_g of $40\,\mathrm{keV}$ pro-

741   tons in the $z = 0$ plane near Ganymede for case (ii). The gyroradii are calculated un-

742   der the "worst-case" assumption, that is, a pitch angle of $\alpha = 90°$. As can be seen, the

743   gyroradius is $r_g = 0.1 R_G$ or less everywhere within approximately $1 R_G$ altitude (red

744   circle), below which the vast majority of the ENA flux into the patch is generated (cyan

745   line in Figure 4(a)). Outside of the $z = 0$ plane, the gyroradii under $1 R_G$ altitude ex-

746 ceed $r_g = 0.1R_G$ only in highly localized regions. Therefore, in the region of ENA gen-

747 eration for the patch feature, the distance between a parent proton and its guiding cen-

748 ter is typically very small compared to the extent of the different magnetospheric regions,

749 and the error associated with our tracing method for the field lines has minimal impact

750 on our classification.

751 Figure 4(a) displays the radial distribution of the ENA flux emitted into the patch

752 by protons on open (navy), closed (orange), and Jovian (green) field lines. In each al-

753 titude bin, the sum of these three histograms is equal to the flux represented by the cyan

754 histogram. ENA production on Jovian magnetospheric field lines (green in Figures 4(a)

755 and 4(b)) represents only a very minor portion of the flux emitted towards the patch fea-

756 ture. Given that the Jovian field lines only thread the atmosphere at high altitudes (above

757 $1R_G$), the neutral density they encounter is too low to drive any considerable ENA pro-

758 duction. Therefore, protons must be magnetically connected to Ganymede to produce

759 substantial ENA flux toward the patch feature in Figure 3.

760 Integration of the three curves reveals that only 25% of the ENA flux emitted into

761 the patch feature (Figure 3) is generated in the closed field line region. As illustrated

762 by the orange curve, ENA production in this region peaks at altitudes of $1,100$–$1,200\,\mathrm{km}$

763 (0.42–$0.46R_G$), and the emissions produced on closed field lines occur entirely below $1R_G$

764 altitude. The ENA flux generated in the closed field line region (orange) follows a sim-

765 ilar behavior with altitude as the total population (cyan). However, in contrast to the

766 full population, the limited extent of the closed field line region (orange in panel 4(b))

767 prevents ENA production on closed field lines beyond $1R_G$ from the surface.

768 The ENA emissions from open field lines contributing to the patch feature exhibit

769 a slight peak at $2,500\,\mathrm{km}$ ($\approx 1R_G$) from the surface, and then level off to a nearly con-

770 stant value down to altitudes of just $300\,\mathrm{km}$ ($\approx 0.1R_G$). As will be discussed below, the

771 vast majority of these ENAs are produced immediately north or south of the OCFB. In

772 these regions, the open field lines (navy in panel 4(b)) are mostly parallel to the $z =$

773 0 plane. Hence, protons gyrating around such field lines with pitch angles away from $90°$

774 may emit ENAs toward the patch feature anywhere between the surface and the top of

775 the atmosphere.

776 Figure 5 displays the longitudinal and latitudinal distribution of the ENA flux con-

777 tributing to the patch feature, analogous to the quantity shown in Figure 4(a). To pro-
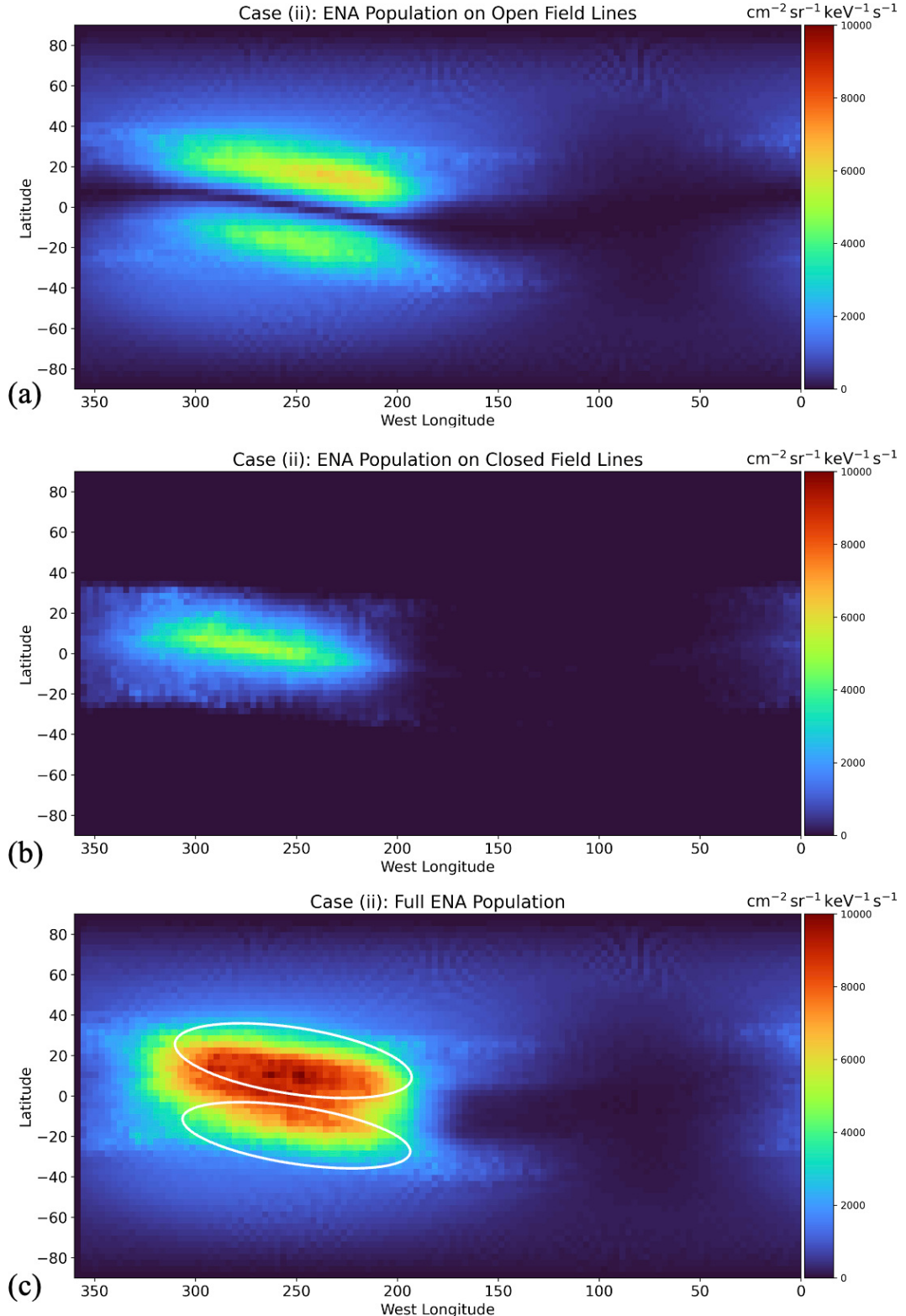
Figure 5. Two-dimensional projections of the total ENA flux emitted into the patch feature (see Figure 3) at an initial proton energy of 40 keV. The ENA population shown here is the same as in Figure 4(a). Analogous to Figure 4(a), these maps do *not* show where ENA flux is recorded on the detector (Figures 1 and 2), but rather demonstrate where the ENA flux is *produced*. The ENA flux generated at *all* altitudes within each longitude and latitude increment is combined into a single bin: the vertical axis of each panel represents the latitude where the ENA flux originates, and the horizontal axis represents the West Longitude. The bin size in each histogram is 3° × 3°. Panel (a) shows the location of ENA emissions from protons on open field lines. Panel (b) displays the locations of ENA flux originating on closed field lines. Panel (c) illustrates the ENA flux produced at each longitude and latitude by all parent protons contributing to the patch, regardless of the type of field line on which they are located. In panel (c), the approximate locations of the dual "stripe" features from panel (a) are indicated by the white ovals. The very minor contribution of ENA flux generated on Jovian field lines (see Figure 4(a)) is not shown here individually, but is still included in panel (c).

778 duce the maps in Figure 5, the ENA fluxes toward the patch, generated in the moon's

779 neutral envelope, are grouped into longitude and latitude bins ($3° \times 3°$) using the an-

780 gular coordinates of each parent proton at the moment of charge exchange. That is, ENAs

781 produced at different altitudes, but at the same longitude and latitude, are assigned the

782 *same* bin. Once again, distinct ENAs emitted sequentially into the patch by the same

783 proton macroparticle are counted separately. Similar to Figure 4(a), we decompose the

784 angular positions of the emitted ENA fluxes $|\mathrm{d}J|$ into those generated on open, closed,

785 or Jovian field lines. Panels 5(a) and 5(b) respectively display the distribution of the ENA

786 flux produced in Ganymede's atmosphere on open and closed field lines, decomposed by

787 latitude and West longitude. Panel 5(c) shows the ENA flux distribution for the full con-

788 tributing proton population. The weak fluxes generated on Jovian field lines (green line

789 in Figure 4(a)) are clustered around equatorial latitudes, but the corresponding map is

790 not included in Figure 5 or our subsequent analysis. We emphasize again that, in con-

791 trast to Figures 1–3, the maps in Figure 5 do *not* display the distribution of the ENA

792 flux through the spherical detector: they rather illustrate the distribution of this flux in

793 the ENA generation region within Ganymede's atmosphere, that is, *before* the ENAs even

794 travel toward the detector sphere.

795   Figure 5(c) demonstrates that the overwhelming majority of the ENA flux emit-

796 ted into the patch is generated in the low-latitude region of Ganymede's trailing hemi-

797 sphere. This cluster of ENA generation is located between longitudes of $200°$–$300°$ W,

798 and it is slightly tilted with respect to Ganymede's equator. Hence, the ENAs forming

799 the patch feature on the detector (Figure 3) are produced directly "below" it in the moon's

800 atmosphere, implying that this population of ENAs has significant velocity components

801 in the radial direction. As illustrated in panels 5(a) and 5(b), the concentrated ENA gen-

802 eration decomposes into two separate features. A pair of "stripes" representing intense

803 ENA generation are formed north and south of the OCFB, created by protons on open

804 field lines (Figure 5(a)). The ENA production in these two stripes exceeds its surround-

805 ings by a factor of 5. The two stripes of slightly elevated ENA flux (visible as yellow in

806 Figure 3) recorded on the detector sphere are located at similar latitudes as these two

807 stripes of ENA *production*. Separating the stripes is a thin, equatorial gap where the gen-

808 erated ENA flux rapidly drops to zero since no open field lines thread the atmosphere

809 at equatorial latitudes (see Figure 4(b)). A narrow stripe of elevated ENA flux is pro-

810 duced by protons on closed field lines around the equator, filling the gap between the

two ENA production regions on open field lines (Figure 5(b)). The flux generated in this
feature only reaches a similar value to the stripes in Figure 5(a) along its center.
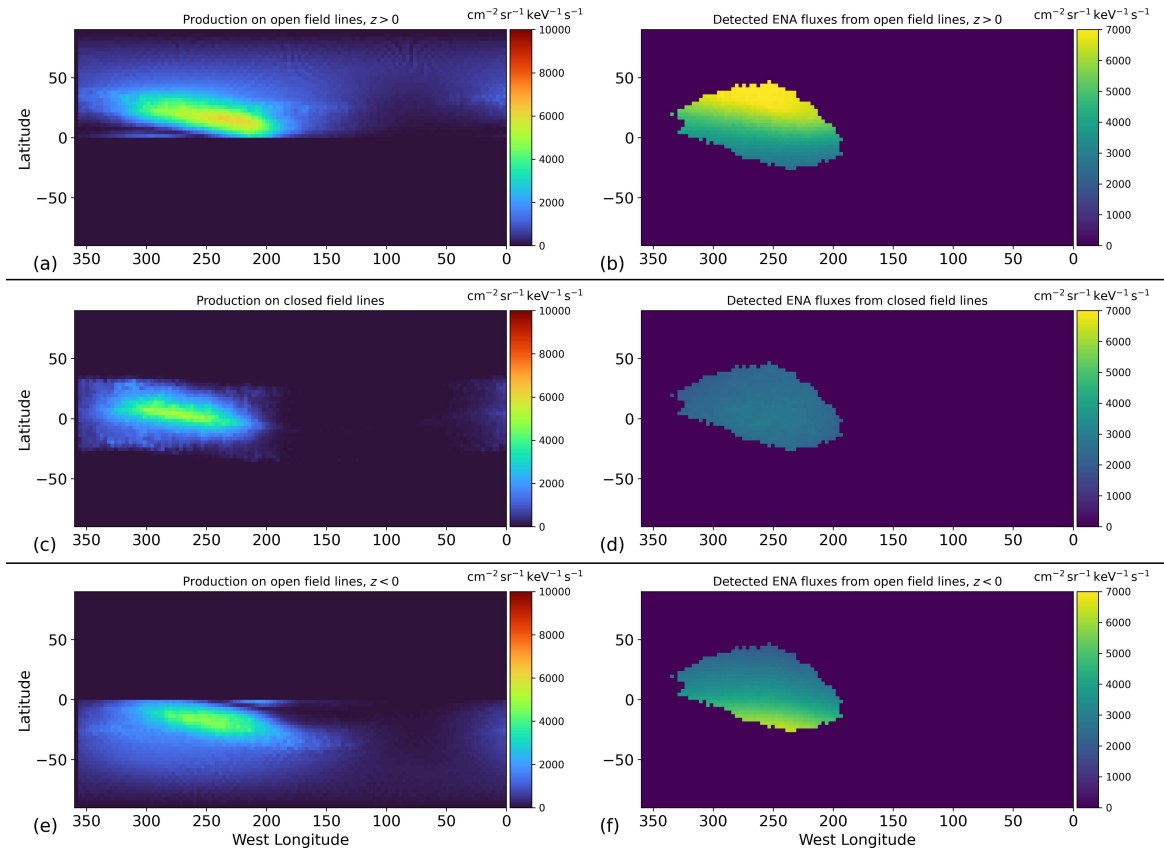
Figure 6. Connection between production and detection of ENAs from the "stripe" features. The panels in the left column display the decomposition of ENA production by longitude and latitude (see Figure 5). However, the "dual stripe" feature from Figure 5(a) is now separated into the contributions from the northern ($z > 0$, panel (a)) and southern ($z < 0$, panel (e)) hemispheres. ENA production on closed field lines is illustrated in panel (c), which is identical to Figure 5(b). The three panels in the right column illustrate the contributions of these three production regions to the flux through the patch on the detector sphere at $|\mathbf{r}| = 3R_G$: (b) detected flux from the northern stripe, (d) flux observed from the central stripe, and (f) flux produced in the southern stripe.

To further elucidate the connection between the three stripes of elevated ENA production in Figure 5 and the patch feature on the detector, Figure 6 displays the contributions of the three individual stripes to the ENA flux through the detector sphere. This decomposition takes into account that the "northern" stripe of ENA production in Fig-

ure 5(a) is confined to the $z > 0$ half space, whereas the "southern" stripe is completely produced in the $z < 0$ half space. The left column of Figure 6 shows the features in the ENA production region, whereas the right column illustrates the corresponding signatures on the detector at $|\mathbf{r}| = 3R_G$ (see also Figure 3).

As can be seen from the top row of Figure 6, ENAs generated on open field lines in the northern hemisphere ($z > 0$) largely contribute to the northern portion of the detected patch feature. In the same way, ENAs emanating from the southern stripe mainly populate the southern segment of the detected patch (Figures 6(e)-(f)). In other words, ENAs produced along an open field line on a certain side of Ganymede's equator tend to remain on the same side for detection. Such ENAs can be emitted from an open field line in several ways: for example, protons with pitch angles near $\alpha \approx 90°$ can produce them at high altitudes where the field vectors are nearly parallel to $\mathbf{B}_0$ (see Figure 4(b)). In addition, protons traveling *along* the field lines may generate them in the region where the field vectors are nearly horizontal (Figure 4(b)). In order for ENAs from the latter group to reach the detector, their parent protons must move *away* from Ganymede. This could happen, for instance, to a proton that approaches the moon along an open field line and gets mirrored back by the strong field near the surface. As shown in the middle row of Figure 6, ENAs produced in the region of closed field lines uniformly populate the entire patch feature on the detector. Hence, there does not appear to be a preferred range of pitch angles at which protons on closed field lines contribute to the patch. However, further investigating the involved mechanisms would require analyzing detailed particle statistics, and we refrain from doing this here.

Both our ENA emission model and AIKEF assume Ganymede's O_2 and H_2 atmospheric densities to depend only on altitude, but not on latitude or longitude. Nevertheless, global asymmetries in the atmospheric densities of these constituents have been proposed by modeling work and HST observations (e.g., Leblanc et al., 2017, 2023; Roth et al., 2021). The intensity of the "patch" feature from Figure 3 may vary for different atmospheric distributions. However, we defer the investigation of that dependence to a follow-up study (see section 2.1). We also emphasize that our discrimination between open and closed field lines refers to the momentary position of a proton at the instant of ENA emission. However, it does not indicate whether a proton remains trapped in the closed field line region for an extended period of time. Isolating the role of quasi-trapped protons would require us to trace many of the proton macroparticles long after their ENA

emission capability has been exhausted. It would also require establishing robust criteria on the residence time of a proton in the closed field line region to determine whether it is quasi-trapped or not (e.g., Liuzzo et al., 2024). For this reason, we refrain from including such an analysis here. A more in-depth investigation might reveal an additional difference between ENA production by quasi-trapped and untrapped protons.

Maps of the ENA emissions through the detector sphere in draped electromagnetic fields (case (iii)) are depicted in the right columns of Figures 1 and 2. Comparison of the three columns (cases (i), (ii), and (iii)) illustrates that the modifications to the ENA emission pattern introduced by the moon's internal dipole field are far more substantial than those imparted by the additional inclusion of the plasma interaction. When the fields are draped, the ENA emission pattern is roughly uniform across the spherical detector: for all initial proton energies, the recorded ENA fluxes vary by only 50%–70% between the respective minimum and maximum. At most longitudes, the ENA flux intensity is slightly reduced in the equatorial region of the detector (see, e.g., panel 2(l)). In order to quantify the modifications to the ENA emission pattern driven by field line draping, Figures 7(a)–(d) display the percent difference in the ENA flux recorded at every detector location between cases (ii) and (iii). That is, blue regions in panels 7(a)–(d) indicate locations where the plasma interaction *reduces* the recorded ENA flux on the detector, white regions imply no change, and red regions represent locations where the detectable ENA flux is enhanced by draping. The ENA emissions directed towards the patch feature on the detector's upstream hemisphere (e.g., Figure 3) are reduced up to 60% when draping is included. In contrast, the ENA fluxes recorded near the detector's downstream apex are only slightly affected, with changes ranging from a drop of roughly 30% at initial proton energies of $10\,\mathrm{keV}$ to approximately 0% above energies of $40\,\mathrm{keV}$.

In order to explain these modifications, we depict the magnetic field strength $|\mathbf{B}|$ near Ganymede for the $y = 0$ plane in the right column of Figure 7, with case (ii) shown in panel (e) and the AIKEF output for case (iii) depicted in panel (f). Comparing these two plots isolates the changes imposed by the plasma interaction on the magnetic field magnitude. Pileup of the Jovian magnetospheric field lines increases $|\mathbf{B}|$ by more than a factor of 2 above Ganymede's upstream apex (see yellow and pink regions around $x \approx -1.5R_G$). In case (ii), the vast majority of ENA flux emitted towards the patch feature is produced in the upstream hemisphere, as indicated by Figure 5(c). The enhanced magnetic field strength in this region makes it less accessible to the incoming ion population:
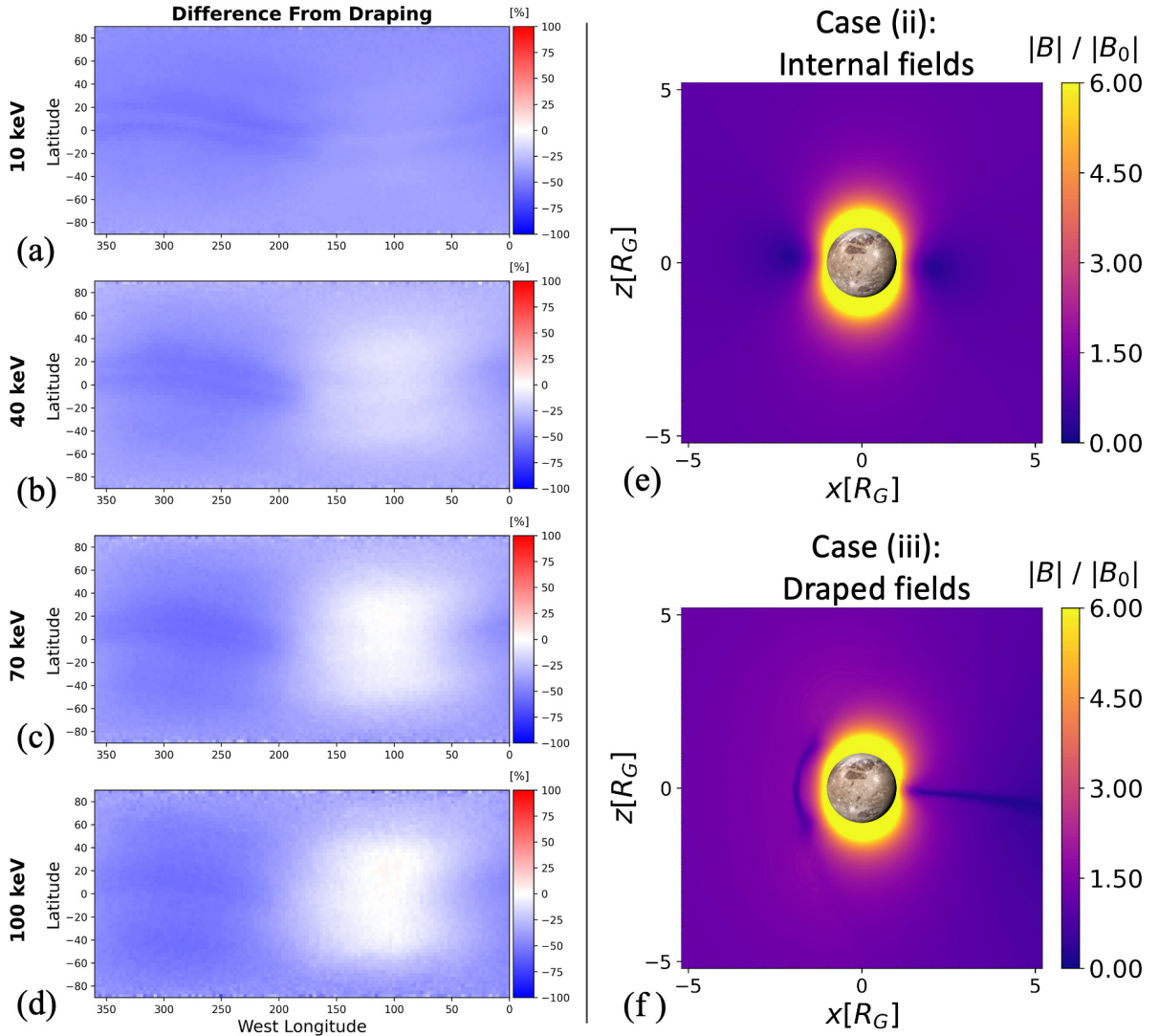
Figure 7. Influence of Ganymede's plasma interaction on the ENA emissions. Panels (a-d) illustrate the percent difference between the ENA flux recorded on the spherical detector for cases (ii) and (iii), that is, the percent change in the ENA flux through every location on the detector when the plasma interaction is included. Panels (a-d) were calculated by subtracting the flux maps in the center column of Figures 1 or 2 from those in the right column. Each panel is arranged in the same way as the panels of Figure 1, with latitude on the vertical axis and West Longitude on the horizontal axis. The colorbar in panels (a-d) ranges from -100% (blue) to $+100\%$ (red). Thus, blue indicates locations where draping reduces the ENA flux, and any (faint) red represents locations where draping enhances the ENA flux. Panels (e) and (f) show the magnetic field magnitude $|\mathbf{B}|$ in the $y = 0$ plane for cases (ii) and (iii), respectively. The values of $|\mathbf{B}|$ in panels (e) and (f) are normalized with the ambient Jovian field magnitude $|\mathbf{B}_0| = 80.2\,\mathrm{nT}$ (see section 2.1), and the axes are scaled in units of R_G.

parent protons drifting towards the moon may be deflected away from the atmosphere by the pileup region, as exemplified by the sample trajectory in Figure 8 of Haynes et al. (2023). Furthermore, the reduction in gyroradii due to the enhanced $|\mathbf{B}|$ in the pileup region prevents incoming protons from reaching deep into the atmosphere via gyration. In contrast, the distribution of ENA flux emitted toward the downstream portion of the detector is left mostly unchanged by draping.

At the time of the Juno flyby, Ganymede's sublimation-driven atmospheric bulge of enhanced H_2O density above the subsolar point was located away from the ramside apex. This bulge does not make any discernible contribution to the flux patterns shown in Figures 1 and 2: when this atmospheric component is omitted from the model, the flux maps appear the same (see also section 3.3 and Appendix A).

3.2 ENA Flux Onto Ganymede's Surface

Figure 8 depicts maps of the ENA fluxes from Ganymede's atmosphere impacting the spherical surface at $|\mathbf{r}| = R_G$ in draped electromagnetic fields (case (iii)). The precipitating ENA flux is binned by latitude and West Longitude coordinates ($3°\times3°$) on the moon. Similar to the ENA emissions recorded on the concentric spherical detector in draped fields (right column of Figure 1), the ENA flux onto Ganymede is quasi-uniform across its surface. For every initial proton energy considered (10–100 keV), the standard deviation of the ENA flux distribution across the moon is less than 8% of the average value on the surface. The ENA flux reaching the polar caps is nearly uniform with longitude, but the flux onto the equatorial regions east and west of the upstream apex (longitudes of 170°–250° W and 300°–360° W) is locally enhanced by 20–25% compared to the surroundings.

Near-infrared observations of Ganymede's surface captured by the Very Large Telescope indicate that the abundance of water ice is depleted by approximately 50% in the region around the trailing apex compared to the equatorial leading hemisphere (Ligier et al., 2019). Since magnetospheric particle precipitation plays a critical role in weathering Ganymede's surface (e.g., Johnson & Quickenden, 1997; Hansen & McCord, 2004; Johnson et al., 2004; Fatemi et al., 2016), such a compositional dichotomy may suggest significant variations in particle influx between different longitudes along the equator (Ligier et al., 2019; Paranicas et al., 2021). The observed region of reduced water ice abundance
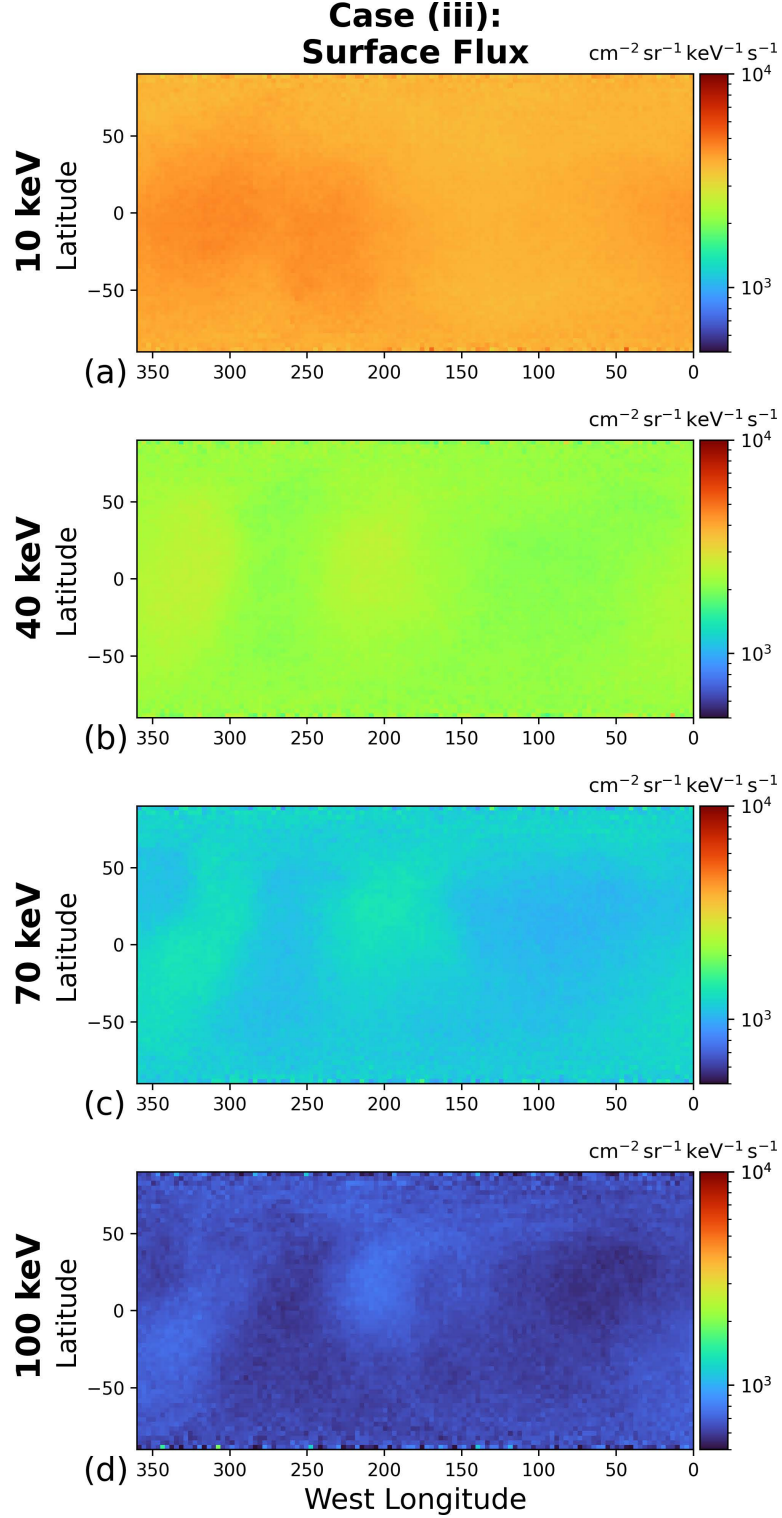
Figure 8. Maps of energetic neutral atom (ENA) fluxes from Ganymede's atmosphere onto the moon's surface (at $|\mathbf{r}| = R_G$) in draped electromagnetic fields (case (iii)). All maps are projected onto a rectangular surface with the West Longitude system, so the upstream apex is located at $270°$ W. The panels correspond to different initial proton energies at launch: $10\,\text{keV}$ in panel (a), $40\,\text{keV}$ in panel (b), $70\,\text{keV}$ in panel (c), and $100\,\text{keV}$ in panel (d). The logarithmic colorscale is the same for all panels, ranging from $5 \cdot 10^2\,[\text{cm}^2\,\text{sr}\,\text{keV}\,\text{s}]^{-1}$ to $1 \cdot 10^4\,[\text{cm}^2\,\text{sr}\,\text{keV}\,\text{s}]^{-1}$.

is located at low latitudes and is covered by closed field lines which largely shield the surface (at all longitudes) from erosion by Jovian ions and electrons (Poppe et al., 2018; Liuzzo et al., 2020). Therefore, Paranicas et al. (2021, 2022) ascribe the difference in water ice abundance to a non-uniform bombardment by ENAs generated via charge exchange in Ganymede's atmosphere. The maps in Figure 8 indicate that, for parent proton energies of 10–100 keV, the ENA influx is slightly enhanced east and west of the upstream apex but remains nearly uniform across the equatorial region at other longitudes. Thus, the morphology of ENA precipitation onto Ganymede is distinct from that of the feature identified by Ligier et al. (2019). In addition, the ENA fluxes onto the surface remain below $6 \cdot 10^3 \, [\mathrm{cm}^2 \, \mathrm{sr} \, \mathrm{keV} \, \mathrm{s}]^{-1}$ at any location (Figure 8). This value may be less than or comparable to the low-latitude influx of magnetospheric *protons* onto the surface (Plainaki et al., 2020; Poppe et al., 2018). Since surface alteration does not depend on the charge state of the projectile, our results do not immediately support a correlation between the observed distribution of surface ice (Ligier et al., 2019; Paranicas et al., 2021) and the ENA precipitation patterns (Figure 8).

Energetic protons that reach Ganymede's surface without undergoing charge exchange may produce backscattered or sputtered ENAs. Between energies of 10–100 keV, the hydrogen ENA flux backscattered from the moon's surface exceeds that generated via sputtering by about an order of magnitude (Pontoni et al., 2022; Szabo et al., 2024). As will be shown in the following, the backscattered ENA fluxes themselves are greatly exceeded by the ENA emissions from the atmosphere across this energy interval. We note that the fluxes of backscattered ENAs provided by Szabo et al. (2024) are given as a function of the ENAs' energies when released from the surface. In contrast, our model calculates flux maps for certain initial *proton* energies on the launch grid. The energy of a parent proton may change as it travels through the non-uniform electromagnetic fields near Ganymede prior to producing an ENA. Thus, in general, the energies of the ENAs recorded on the spherical detector (or at the surface) are not the same as those of their parent protons at launch. However, we found that the energy of most parent protons at the instant of ENA generation deviates only slightly from their launch energy: for example, at an initial proton energy of 40 keV, more than 86% of the emitted ENAs have energies within ±10% of 40 keV. This result is similar to the findings of Nordheim et al. (2022) for Europa: energetic protons only experience a minor change of their velocity

946   magnitude as they travel through the draped electromagnetic fields near that moon (see

947   Figure 13 in their study).

948   Averaged over Ganymede's surface, the backscattered ENA flux ranges from $5 \cdot$

949   $10^1 \, [\text{cm}^2 \, \text{sr} \, \text{keV} \, \text{s}]^{-1}$ to $1{\cdot}10^{-1} \, [\text{cm}^2 \, \text{sr} \, \text{keV} \, \text{s}]^{-1}$ across the considered energy range (10–

950   100 keV, see Szabo et al., 2024). In comparison, the average value of the ENA flux emit-

951   ted from Ganymede's atmosphere through the concentric detector varies from $2{\cdot}10^4 \, [\text{cm}^2 \, \text{sr} \, \text{keV} \, \text{s}]^{-1}$

952   at an initial proton energy of 10 keV to $1{\cdot}10^3 \, [\text{cm}^2 \, \text{sr} \, \text{keV} \, \text{s}]^{-1}$ at 100 keV (case (iii) in

953   Figures 1 and 2). Therefore, in the keV regime, the hydrogen ENA fluxes backscattered

954   from the surface are orders of magnitude weaker than the fluxes emitted by charge ex-

955   change in the moon's atmosphere. Hence, above energies of a few keV and within the

956   range of JENI (0.5–300 keV for hydrogen; see Galli et al., 2022), we expect the emissions

957   produced in Ganymede's neutral envelope to be the main contributor to the ENA im-

958   ages taken by JUICE. However, this assessment also depends on the viewing geometry.

959   For instance, during a close flyby, the bulk of Ganymede's atmosphere would reside out-

960   side the FOV of the instrument. Hence, a detector pointing toward the surface may still

961   be suitable to capture discernible fluxes of sputtered and backscattered ENAs. Also, Fig-

962   ure 8 reveals that for the energies considered, the hydrogen ENA flux emitted from the

963   moon's atmosphere onto its surface substantially exceeds the flux released from the sur-

964   face.

965   ### 3.3 Synthetic ENA Images of Ganymede's Mini-Magnetosphere

966   Figure 9 displays synthetic ENA images of Ganymede's interaction region for the

967   conditions during the Juno PJ34 flyby. Six separate viewing geometries are represented

968   by the different panels (a-f), with the images on the left showing the emissions for uni-

969   form fields (case (i)) and the images on the right corresponding to the superposition of

970   the Jovian background field $\mathbf{B}_0$ with Ganymede's internal field (case (ii)). Synthetic ENA

971   images from detectors positioned upstream and downstream of Ganymede at $\mathbf{r} = (\mp 4 R_G, 0, 0)$

972   are shown in panels 9(a) and 9(d), those captured above the moon's anti-Jovian and sub-

973   Jovian apices at $\mathbf{r} = (0, \mp 4 R_G, 0)$ are displayed in panels 9(b) and 9(e), and images

974   taken south and north of the moon at $\mathbf{r} = (0, 0, \mp 4 R_G)$ are in panels 9(c) and 9(f), re-

975   spectively. We adopt the layout of the synthetic ENA images used by Haynes, Tippens,

976   et al. (2025) to facilitate comparison to their results for Europa and Callisto; that is, the

977   azimuthal coordinate of the detector's FOV in each image is on the vertical axis, and el-
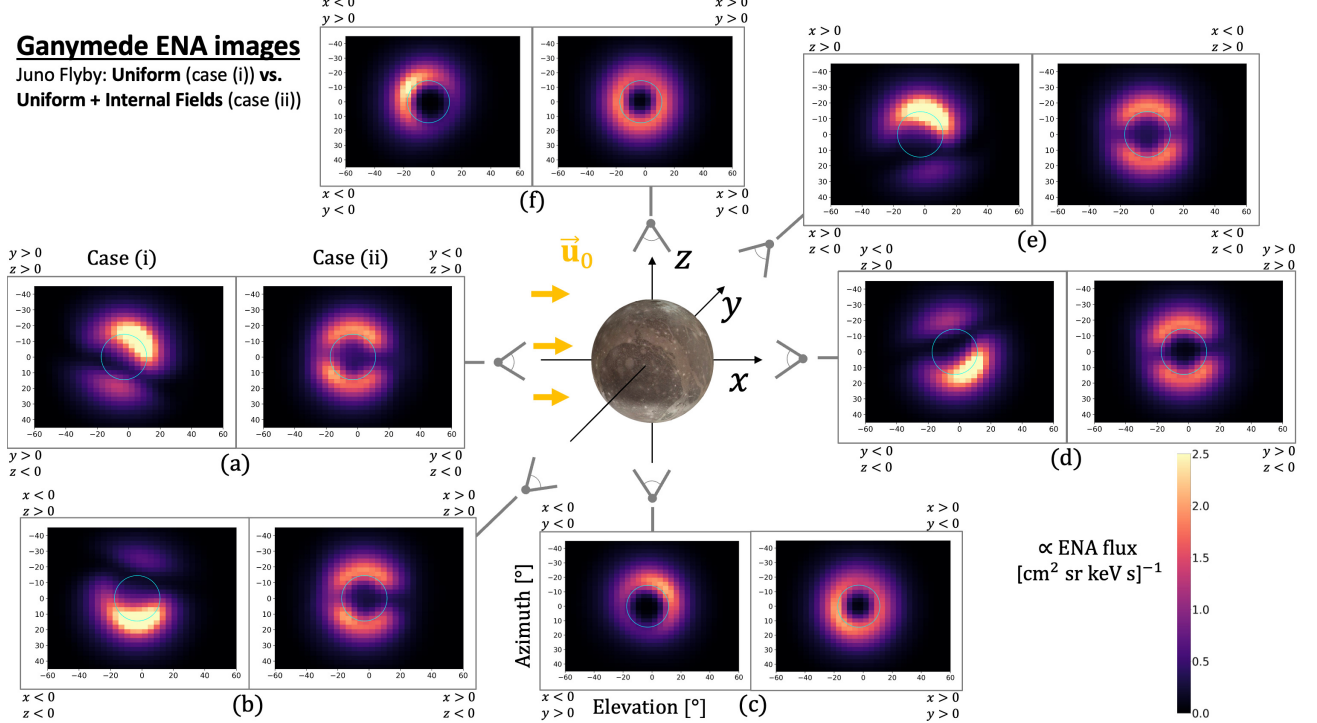
Figure 9. Synthetic ENA images, calculated for uniform fields (case (i)) and Ganymede's internal field superimposed with the ambient Jovian field (case (ii)) on the left and right sides of each panel, respectively. The ENA images are arranged with detector elevation on the horizontal axis and detector azimuth on the vertical axis. Ganymede's disc is illustrated by the blue circle in each subplot. The direction of the upstream plasma flow $\mathbf{u}_0$ is represented by the yellow arrows. For each synthetic ENA image, the detector is located at $|\mathbf{r}| = 4R_G$, and the boresight vector points radially towards the center of Ganymede. The gray symbol connected to every panel represents the detector, pointing at the moon with its boresight vector parallel or antiparallel to a coordinate axis of the GPhiO system. In panels (a) and (d), the detectors are located along the x axis at $(\mp 4R_G, 0, 0)$ with the boresight vectors $(\pm 1, 0, 0)$. In panels (b) and (e), the detectors are positioned on the y axis at $(0, \mp 4R_G, 0)$ with boresight vectors of $(0, \pm 1, 0)$. In panels (c) and (f), the detectors are positioned along the north-south axis at $(0, 0, \mp 4R_G)$ with boresight vectors given by $(0, 0, \pm 1)$. The labels in the corners of each image denote which quadrants of the GPhiO system are visible in the quadrants of the images. The values of the ENA flux for our chosen timestep (see section 2.3 and Haynes, Tippens, et al., 2025) are given by the colorbar in the lower-right corner.

evation is on the horizontal axis. This format is also frequently used in the literature on ENA observations from the Cassini mission (see, e.g., Tippens, Roussos, et al., 2024, and references therein). In every panel, the detector is positioned at a distance of $|\mathbf{r}| = 4R_G$ from the origin of the GPhiO system, and the boresight points radially towards Ganymede's center. Hence, in all images, the angular separation between a LOS running tangent to the moon's disc (blue circle) and the detector's boresight vector is $\beta_G = \arctan(1/4) \approx 14.0°$. Lines of sight forming an angle $\beta < \beta_G$ against the boresight intersect Ganymede's disc. The four quadrants of each synthetic ENA image are labeled to indicate the quadrants of the GPhiO system from which they receive ENA flux. For instance, pixels in the upper-left quadrant of the images in panel 9(b) record ENAs generated in the northern, upstream quadrant of the GPhiO system (i.e., $x < 0$, $z > 0$). As discussed in section 2.3 and Haynes, Tippens, et al. (2025), the synthetic ENA images do not show absolute flux values, but rather a relative brightness pattern (i.e., the image morphology) that is proportional to the absolute values of the ENA flux.
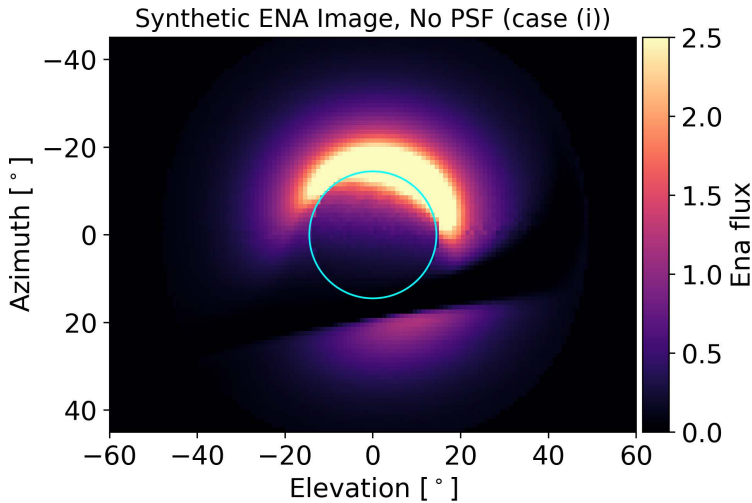
Figure 10. Synthetic ENA image at Ganymede for case (i), captured by the detector above the sub-Jovian apex, *without* the point spread function (PSF) or the downscaling procedure applied. After the post-processing steps, this synthetic ENA image would become the same as the left subplot in panel 9(e).

For uniform Jovian electromagnetic fields (case (i), left subplots in Figure 9), the ENA flux recorded by all six detectors peaks at the edge of Ganymede's disc and drops moving toward its center. To provide context for the analysis of these results, Figure 10

shows the synthetic ENA image captured above Ganymede's sub-Jovian apex for case (i) *without* the PSF and downscaling applied after image generation (see section 2.3 and Haynes, Tippens, et al., 2025). As demonstrated by Figure 10, a large majority of the flux is captured by pixels outside of the moon's disc: the ENA flux recorded by pixels viewing Ganymede's disc is elevated only for a narrow strip at the limb, and it falls rapidly moving towards the center. Prior to the post-processing steps, the other five images for case (i) share a similarly small fraction of ENA flux captured within the disc (not shown). Since the gyroradii of parent protons with energies $10\,\mathrm{keV} \leq E \leq 70\,\mathrm{keV}$ are on the order of $0.1 R_G$, those situated between any of our detectors and the moon may travel tangent to a LOS via their gyromotion. That is, lines of sight forming an angle below β_G against the boresight can be populated by ENAs from protons gyrating between the moon and the detector. This yields the nonzero ENA flux recorded on the moon's disc. The density of the atmospheric column along a LOS intersecting Ganymede's disc decreases moving from the limb towards the center. In consequence, the recorded flux decreases moving towards the center of the disc (see also the results of Haynes, Tippens, et al., 2025, for Europa). The elevated ENA flux appears to populate a larger portion of the disc in Figure 9(e) than in Figure 10 (yellow hues); this "bleedover" of ENA flux into the disc is introduced from neighboring pixels in the limb when applying the PSF (see also Tippens, Roussos, et al., 2024). The same effect occurs in the images taken from the other five detector vantages.

Away from Ganymede's disc, the ENA flux recorded by all six detectors in case (i) falls to approximately zero at azimuths or elevations above $\pm 35°$ (black pixels in Figure 10 and the left subplots of Figure 9). A LOS that connects to these pixels makes an angle of at least $35°$ against the boresight: the minimum altitude pierced by such a LOS is $(4\sin 35° - 1)R_G \approx 1.3 R_G$. At distances above $1 R_G$ from the surface, the extended molecular hydrogen component of the atmosphere is the primary driver of ENA production, since its scale height of $0.38 R_G$ greatly exceeds those of the two other constituents in our model. However, even the H_2 density has fallen by two orders of magnitude at an altitude of $1.3 R_G$ compared to the surface, rendering the atmosphere too dilute to support substantial ENA production.

In all synthetic images obtained for case (i), the ENA flux varies considerably moving around the edge of the moon's disc (Figure 9). For instance, the sub-Jovian detector records an order of magnitude difference between the minimum and maximum val-

ues in the limb, with the majority of the detected ENA flux emanating from above Ganymede's northern polar cap (Figure 10 and left image in panel 9(e)). For the other five vantages, the bulk of the ENA flux similarly populates a cluster of pixels near the edge of the moon's disc, but the locations and angular extensions of the maxima and minima are different than in panel 9(e). Haynes, Tippens, et al. (2025) found a comparable trend in synthetic ENA images for Europa and Callisto when these two moons are at their maximum distances below the center of Jupiter's plasma sheet. In the configurations studied by these authors, the Jovian magnetospheric field $\mathbf{B}_0$ is uniform and inclined against the boresight vectors of all six detectors, which are defined in the exact same way as in Figure 9. Haynes, Tippens, et al. (2025) attributed the asymmetry in their synthetic ENA images to hemispheric differences in the angles between $\mathbf{B}_0$ and the detector's lines of sight. On the side of the disc with elevated ENA flux, a stronger alignment allows parent protons with steep pitch angles to contribute intense fluxes to the image. Due to their smaller gyroradii, such protons can reach the dense, low-altitude portion of the atmosphere where the generated flux is maximized. In the opposite hemisphere, the increased angle between $\mathbf{B}_0$ and the lines of sight requires parent protons to possess pitch angles around $90°$ in order to emit ENAs into the detector. The associated, large gyroradii facilitate absorption of the protons by the moon's surface prior to ENA emission toward the detector. This effect has been analyzed in detail by Haynes, Tippens, et al. (2025, see their Figures 7 and 12). Therefore, we only explain the mechanism generating the ENA flux pattern captured for case (i) by the detector above the sub-Jovian apex (panel 9(e)) as an example, and we refer the reader to our preceding study for a more extensive treatment of other viewing geometries.

In the $x = 0$ plane, Figure 11 illustrates the mechanism that leads to the disparity between ENA flux into the northern and southern segments of the image for uniform fields in panel 9(e). Because the Jovian field $\mathbf{B}_0$ is tilted by only $10.8°$ against the $x = 0$ plane, we assume for the following analysis that $\mathbf{B}_0$ is contained entirely within that plane (analogous to Haynes, Tippens, et al., 2025). Projected onto the $x = 0$ plane (green), $\mathbf{B}_0$ makes an angle of $\eta = 17.7°$ (purple) against the $(-z)$ axis. The range of angles ξ between a LOS outside the disc (blue) and the projection of $\mathbf{B}_0$ onto the $x = 0$ plane (green) is represented by the red elements of the figure. For the angle between the boresight and a LOS, we consider only values $\beta \geq \beta_G$: Figure 10 indicates that the bulk of the ENA flux is recorded by pixels outside Ganymede's disc. A comparison of pan-

els 11(a) and 11(b) demonstrates that the range of ξ values is larger for the southern half-space than for the northern half-space. On each side of the moon, the angle β (magenta) between the detector's boresight vector (in this case, $-\hat{\mathbf{y}}$) and a LOS outside the disc ranges from $\beta_G = 14.0°$ to the maximum azimuth in the detector's FOV, $\beta = 45°$. As demonstrated by Figure 11(a), the angle ξ for a LOS extending into the $z > 0$ half-space is given by $\xi = (90° - \eta) - \beta$: that is, it ranges from $\xi = 27.3°$ for the outermost LOS ($\beta = 45°$) to $\xi = 58.2°$ for the innermost LOS ($\beta = \beta_G$). Conversely, the angle between $\mathbf{B}_0$ and a LOS in the $z < 0$ half-space is given by $\xi = (90° - \eta) + \beta$, ranging from $\xi = 86.3°$ at $\beta = \beta_G$ to $\xi = 117.3°$ at $\beta = 45°$ (see Figure 11(b)).

A parent proton must momentarily travel antiparallel to a LOS in order to emit ENA flux into the detector pixel at its footpoint. In the energy range considered, the velocity $\sqrt{2E/m_p}$ of the protons exceeds the drift velocity $|\mathbf{u}_0|$ by at least an order of magnitude. Therefore, our analysis considers only the protons' translation (along $\mathbf{B}_0$) and gyromotion. Hence, the range of ξ values in either half-space matches the range of pitch angles α for the parent protons that can populate the $z < 0$ or $z > 0$ segment of the image with ENA flux. Protons emitting ENA flux along a LOS extended into the $z > 0$ half-space have pitch angles of $\alpha \in \{27.3°, 58.2°\}$, whereas the pitch angles are given by $\alpha \in \{86.3°, 117.3°\}$ for protons connecting to a LOS in the $z < 0$ half-space. The parent protons approaching a LOS in the $z > 0$ half-space arrive from the north with gyroradii $r_g = \sqrt{2Em_p} \sin\alpha / (e|\mathbf{B}_0|)$ that range between 46% and 85% of their maximum values at $\alpha = 90°$. In the uniform fields of case (i), the majority of the ENA flux is produced at low altitudes, recorded by pixels immediately adjacent to the moon's disc (see Figures 9 and 10). Since $\mathbf{B}_0$ makes a smaller angle against the lines of sight in the $z > 0$ hemisphere than for $z < 0$, the protons emitting ENAs into the $z > 0$ portion of the detector have smaller gyroradii and can penetrate more deeply into Ganymede's atmosphere than those emitting towards the $z < 0$ segment. Moreover, the steeper pitch angles in the $z > 0$ half-space correspond to fewer gyrations within the atmosphere and a reduced path length taken through the neutral gas (see also discussion of the band of elevated ENA flux in section 3.1). Hence, when reaching a LOS with $z > 0$ to emit an ENA, many of the proton macroparticles have retained a larger fraction of their initial flux J than in the southern hemisphere where α is closer to $90°$.

To access lines of sight in the $z < 0$ half-space, protons with pitch angles of $\alpha \in \{86.3°, 90°\}$ approach from north of Ganymede, while protons that have pitch angles in
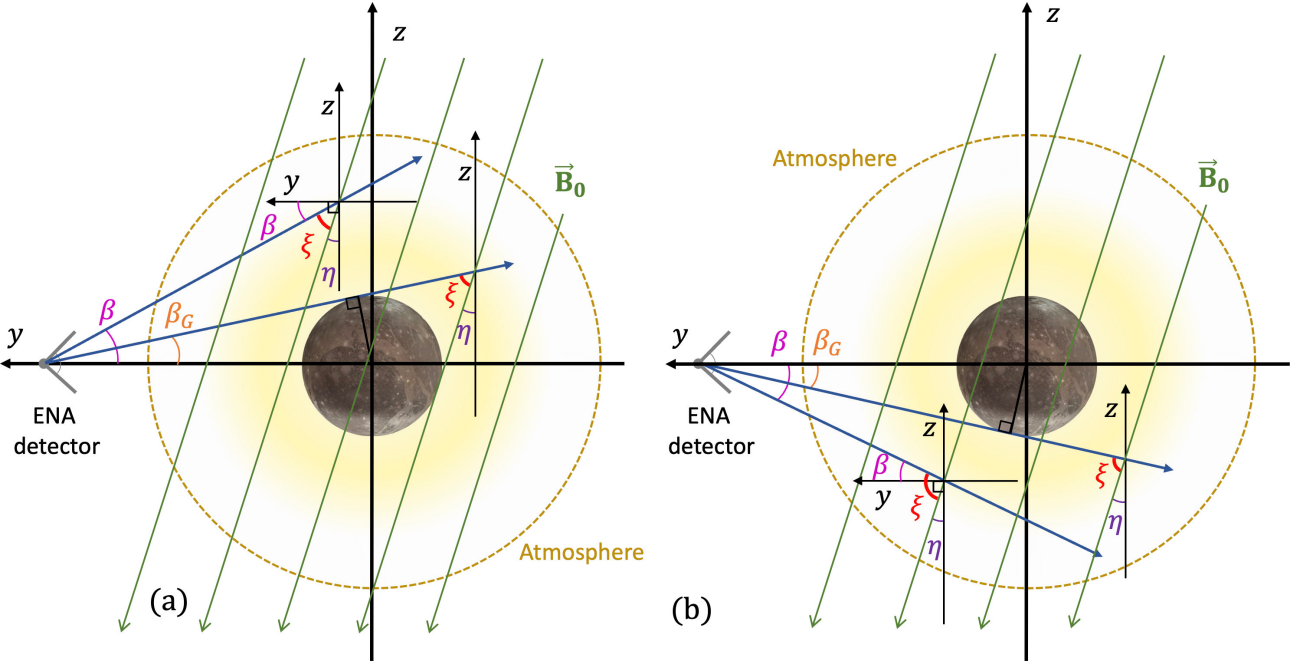
Figure 11. Schematic illustrating the difference in the range of angles ξ between $\mathbf{B}_0$, projected onto the $x = 0$ plane, and the lines of sight (blue) extended into the northern (panel (a)) or southern (panel (b)) half-space from the detector positioned above Ganymede's sub-Jovian apex. This configuration corresponds to the synthetic ENA image in the left sub-panel of Figure 9(e). The projected Jovian field $\mathbf{B}_0$ is represented by the green lines. The minimum opening angle β_G between the boresight and a LOS running tangent to the moon's disc is shown in orange. Another LOS, forming a larger angle $\beta \in \{\beta_G, 45°\}$ against the boresight is shown in magenta. The value of β is limited by the range of the azimuthal coordinate in the detector's FOV ($\pm 45°$). The tilt angle $\eta = 17.7°$ of the projected Jovian field against the ($-z$) axis in planes of constant x is shown in dark purple. The detector is represented by the gray elements, and the upper boundary of Ganymede's atmosphere in the model is conveyed by the dashed yellow circle. The diagram is not to scale.

the range $\alpha \in \{90°, 117.3°\}$ come from the south. We first discuss the population that impinges from the north. In order to even reach a LOS in the $z < 0$ half-space, these protons first must avoid impacting Ganymede. Hence, their guiding centers need to remain above the moon's surface by at least one gyroradius. With pitch angles near $90°$, the gyroradii of such protons range from 0.07–$0.18 R_G$, i.e., they are larger than those of protons that also approach from the north but contribute to the $z > 0$ portion of the image. Therefore, parent protons traveling southward in the $z < 0$ hemisphere have

a higher likelihood of gyrating into the moon prior to emitting ENAs along a LOS than those contributing at $z > 0$. In addition, protons reaching a LOS in the $z < 0$ half-space take a more extended path through the atmosphere than those shaping the $z > 0$ part of the image; at a given energy, their velocity vectors possess a smaller component along $\mathbf{B}_0$, thereby increasing the number of gyrations within the atmosphere prior to emitting an ENA along a LOS. Hence, the fraction of their initial flux J that they still carry when arriving at the LOS is lower than for protons with $z > 0$.

In contrast, protons that arrive from the south do not need to bypass Ganymede before reaching the $z < 0$ lines of sight. However, these particles can emit ENAs only along a LOS with an angle against the boresight larger than $\beta = \eta$ (Figure 11(b)), corresponding to a minimum altitude for emissions at $(4\sin\eta - 1)R_G \approx 600\,\mathrm{km}$. At this altitude, the atmospheric O_2 density has already fallen by an order of magnitude compared to the surface. Even though the H_2 density has only dropped by a factor of two at $600\,\mathrm{km}$ above the surface, this component constitutes less than a third of the total atmospheric column density. Thus, the ENA flux generated by protons approaching from the south makes only minor contributions to the synthetic images, visible in the cluster of pixels that record the weak intensities south of Ganymede's disc (purple in Figure 10). For these reasons, higher ENA fluxes are detected in the northern ($z > 0$, yellow) portion of the image than in the southern ($z < 0$, purple) segment for the detector above Ganymede's sub-Jovian apex (panel 9(e) and Figure 10).

The detector positioned above Ganymede's anti-Jovian apex (panel 9(b)) records elevated ENA flux only in the southern hemisphere. In this configuration, the trend illustrated by Figure 11 is reversed: the ambient magnetic field lines are more closely aligned with lines of sight in the southern half-space than in the north, yielding enhanced ENA flux into the detector from $z < 0$ compared to $z > 0$. The non-uniform ENA flux around Ganymede's disc for the other four detector positions in case (i) can largely be explained in an analogous way as depicted in Figure 11. As shown in Appendix A, *none* of the asymmetries visible in the case (i) images of Figure 9 are generated by the non-uniform distribution of H_2O within the moon's atmosphere.

When Ganymede's internal dipole field is included (case (ii)), the morphology of the synthetic ENA images changes substantially compared to perfectly uniform fields (left versus right subplots in Figure 9). Akin to our findings for the ENA emissions through

the global detector sphere (Figures 1 and 2), the peak values of the ENA fluxes in each image for case (ii) are lower than in case (i). All detectors in the equatorial plane (panels 9(a), 9(b), 9(d), and 9(e)) record a similar pattern: two crescents of elevated ENA flux are located above the northern and southern edges of the moon's disc, separated by two gaps of reduced flux at equatorial latitudes. In contrast, the detectors positioned above the north and south poles record an approximately uniform ring of elevated ENA flux around Ganymede's disc (panels 9(c) and 9(f)).

The morphology of the synthetic ENA images for case (ii) is controlled largely by Ganymede's internal field. For detectors in the equatorial plane, the gaps of reduced ENA flux around $z = 0$ coincide with the region of closed field lines that covers the moon's low-latitude surface (see Figure 4(b)). As demonstrated by Figures 4(a) and 5, the fraction of ENA flux generated within the closed field line region is small compared to the flux produced by protons on open field lines at higher latitudes. This leads to the gaps in ENA flux across Ganymede's equatorial region in Figures 9(a), 9(b), 9(d), and 9(e). A larger number of protons can emit ENAs into these detectors from the open field lines connecting to the moon's polar caps (see also Figures 4(a) and 5). This produces the crescents of enhanced ENA flux for these four detector geometries in case (ii).

Conversely, the detectors positioned to the moon's north and south at $\mathbf{r} = (0, 0, \pm 4R_G)$ cannot perceive the latitudinal separation between open and closed field lines from their vantage. Open field lines occupy the locations directly poleward of the closed field line region (see Figure 4(b)). Hence, in contrast to the detectors positioned within Ganymede's equatorial plane, a LOS extending from either detector above the poles inevitably pierces through open field lines before and after intersecting the region of closed field lines. Therefore, decreased proton access to the closed field line region (see also Cooper et al., 2001; Poppe et al., 2018) only slightly reduces the ENA flux along such a LOS. Since this happens at all longitudes where lines of sight from the detectors at $\mathbf{r} = (0, 0, \pm 4R_G)$ intersect the atmosphere, a complete ring of elevated ENA flux around the moon's disc is present in the images (Figures 9(c) and 9(f)).

For case (ii), the ENA emission morphology recorded by the two detectors at $\mathbf{r} = (\pm 4R_G, 0, 0)$ is slightly rotated with respect to the north-south axis. This effect is most evident for the detector located downstream of Ganymede (panel 9(d)), where the crescents of elevated ENA flux are rotated counterclockwise around the boresight (pointing

1165   into the plane of the figure). This subtle tilt stems from the inclination of $\mathbf{B}_0$ against

1166   the $y = 0$ plane. Even when Ganymede's internal dipole is included, the effect of the

1167   positive $B_{0,y}$ component is visible in the orientation of the open field lines above the po-

1168   lar caps (navy in Figure 4(b)). In case (ii), the majority of the detectable ENA emis-

1169   sions are produced by protons on open field lines. The positive $B_{0,y}$ component causes

1170   a counterclockwise rotation of the field lines and proton gyroplanes around the boresight

1171   (i.e., anti-parallel to the x-axis). This rotation maps into the observable ENA emission

1172   morphology (right image of panel 9(d)). In the same way, the positive $B_{0,y}$ component

1173   drives a slight, clockwise tilt in the morphology of the synthetic ENA image captured

1174   from upstream (panel 9(a)).

1175   Synthetic ENA images for draped electromagnetic fields (case(iii)) are shown in the

1176   right subplots of Figure 12. They are compared to the results for the superposition of

1177   Ganymede's internal field with $\mathbf{B}_0$ (case (ii)) in the left subplots. That is, the left sub-

1178   plots of Figure 12 are identical to the right subplots in Figure 9. The same timestep was

1179   used to generate the results for all three cases. In panels 12(a) and 12(d), the differences

1180   between the synthetic ENA images for case (ii) and case (iii) are largely quantitative,

1181   with no significant changes to the morphology. In contrast, a substantial reduction to

1182   the ENA flux in the region upstream of Ganymede's disc ($x < 0$) is visible in panels

1183   12(b), 12(c), 12(e), and 12(f), representing the only major morphological change intro-

1184   duced by draping.

1185   As described in section 3.1, the compressed magnetic field in Ganymede's ramside

1186   pileup region lowers the accessibility of the upstream atmosphere to the incident par-

1187   ent protons compared to case (ii). Thus, only a fraction of the protons that emit ENA

1188   flux into the detector along a LOS through the pileup region in case (ii) still do so when

1189   the fields are draped (case (iii)). Hence, in all ENA images from case (iii) that are cap-

1190   tured in the $x = 0$ plane, the ENA flux recorded by the pixels upstream of the moon's

1191   disc is reduced compared to its downstream side (panels 12(b), 12(c), 12(e), and 12(f)).

1192   Detectors with boresight vectors along the ($\pm x$)-axis (panels 12(a) and 12(d)) do not per-

1193   ceive this upstream/downstream asymmetry, and these synthetic images exhibit only mi-

1194   nor changes imposed by field line draping. Hence, to maximize the visibility of plasma

1195   interaction signatures in ENA images of Ganymede's atmosphere, the ENA detector's

1196   boresight should be directed perpendicular to the flow-aligned axis. The two Alfvén wings

1197   above Ganymede's polar caps do not leave an immediate imprint in the observable ENA
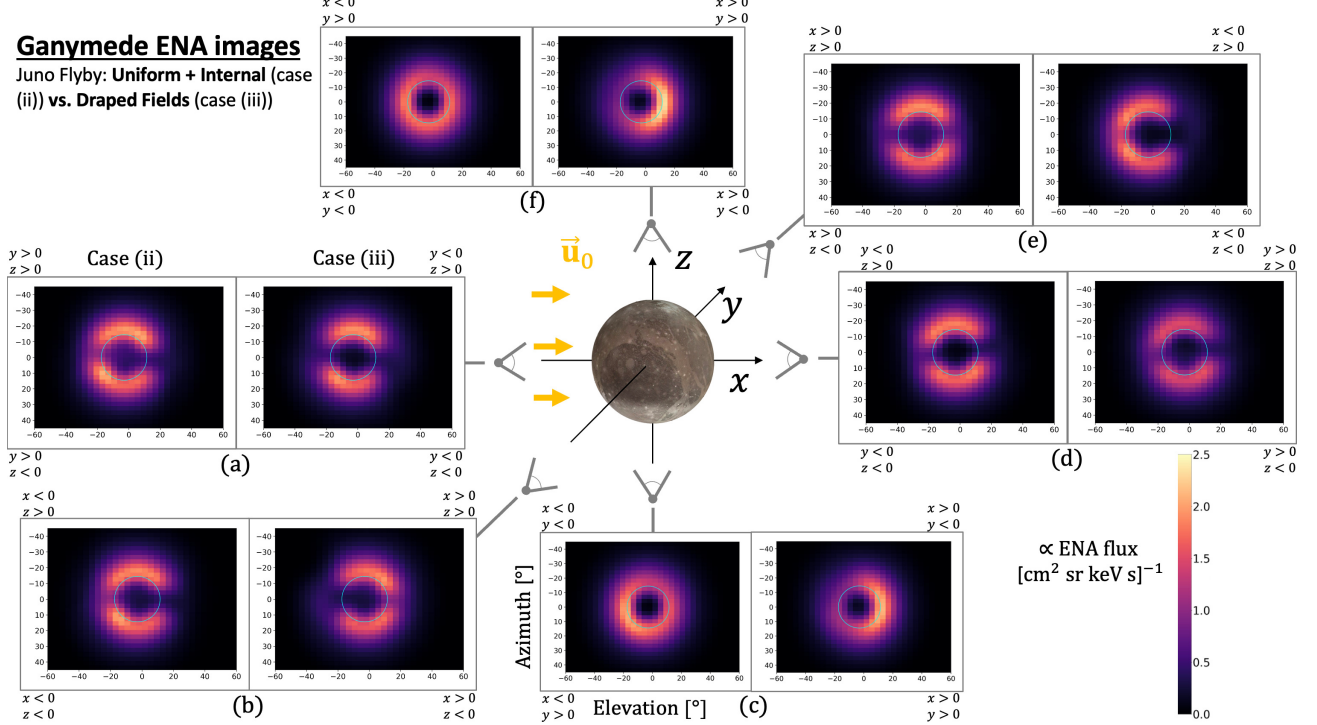
Figure 12. Synthetic ENA images of Ganymede's mini-magnetosphere, without (case (ii)) and with (case (iii)) draped fields from AIKEF included. The layout of the figure is the same as that of Figure 9. The images for cases (ii) and (iii) are shown on the left and right side of each panel, respectively. To facilitate comparison between cases of successively increasing complexity, the synthetic ENA images on the left side of the panels in this figure are the same as those on the right side of the respective panels in Figure 9. For all panels (a-f), detector elevation is on the horizontal axis and detector azimuth is on the vertical axis. In each image, Ganymede's disc is represented by the blue circle. The detector is positioned at a distance of $|\mathbf{r}| = 4R_G$. The corners of every panel are labeled according to the quadrants of the GPhiO System. The gray detector symbol attached to each panel illustrates the viewing geometry in the respective images. The range of the colorscale and the timestep used for these images are the same as in Figure 9.

emission morphology (Figure 12). These structures largely form outside the atmosphere where the density of the neutral gas is too low for substantial ENA generation.

The images captured by detectors in the $x = 0$ plane (i.e., panels 12(b), 12(c), 12(e), and 12(f)) also indicate that the ENA flux emanating from the region above the wakeside apex is slightly elevated in case (iii) compared to case (ii). This increase is consistent with the ion tracing results of Poppe et al. (2018), who found an enhanced en-

ergetic proton accessibility to the region immediately downstream of Ganymede when the fields are draped (see panel (a) in their Figures 7 and 8). We note that any pixels intersecting Ganymede's disk and recording low ENA fluxes in our case (iii) images may be suitable to discern ENA emissions from the surface, generated by sputtering or backscattering.

Overall, Figures 9 and 12 reveal that Ganymede's strong internal field mostly prevents both the uniform Jovian field $\mathbf{B}_0$ and field line draping from leaving a substantial imprint in the ENA images. This is fundamentally different from Europa or Callisto, which possess only weak internal fields due to induction; at these objects, draping can significantly alter the ENA emission morphology (Haynes, Tippens, et al., 2025). Furthermore, our results illustrate that the flux patterns seen by the global, spherical ENA detector (section 3.1) do not immediately map into the synthetic ENA images (section 3.3). Hence, a combination of both approaches is necessary to understand the nature of ENA emissions at Ganymede.

4 Summary and Concluding Remarks

In this study, we constrain the morphology and observability of ENA emissions from charge exchange between energetic magnetospheric protons and Ganymede's atmosphere. In doing so, we provide a "template" to contextualize the ENA images to be taken at Ganymede by the JENI detector aboard JUICE (e.g., Tosi et al., 2024). The ability of ENA images to visualize Ganymede's mini-magnetosphere at a global scale complements local plasma and electromagnetic field observations taken along a spacecraft trajectory.

We combine the electromagnetic field output from the AIKEF hybrid model (kinetic thermal ions, fluid electrons) with tools that calculate the trajectories of energetic protons in Ganymede's environment and determine their contributions to ENA production. The protons are traced at several energies, ranging from $10\,\mathrm{keV}$ to $100\,\mathrm{keV}$. We calculate the ENA flux through a spherical detector of radius $3R_G$ that encloses Ganymede's entire atmosphere. In addition, we determine the ENA flux recorded by a set of point-like detectors, each with a finite FOV that emulates an ENA camera aboard a spacecraft. Our analysis takes into account six (hypothetical) ENA detectors at a distance of $4R_G$ from Ganymede's center, positioned along the $(\pm x)$, $(\pm y)$, and $(\pm z)$ axes of the GPhiO system with their boresight vectors pointing radially toward the moon. For both the de-

tector sphere and the point-like detectors, we examine three cases for the electromagnetic fields near Ganymede at successively increasing complexity: perfectly uniform Jovian fields (case (i)), the Jovian field superimposed with Ganymede's internal dipole field (case (ii)), and draped fields from AIKEF (case (iii)). The upstream conditions used in these configurations represent Ganymede's environment at the time of the Juno PJ34 flyby (Stahl et al., 2023).

Our major findings are as follows:

- For perfectly uniform fields (case (i)), the ENA emissions through the spherical detector display a circular band of elevated flux wrapping around the entire sphere; the normal of this band's plane is parallel to the ambient Jovian field $\mathbf{B}_0$. This structure is largely generated by protons with pitch angles close to $\alpha = 90°$. Synthetic ENA images of Ganymede's interaction region record a localized cluster of elevated ENA flux at the edge of the moon's disc, with the position of this enhancement depending on the viewing geometry. Only weak fluxes can be observed elsewhere around the disc. In the region where the intense ENA flux is generated, a small angle between $\mathbf{B}_0$ and detector's lines of sight leads to reduced proton gyroradii. This allows these ions to reach low altitudes in Ganymede's atmosphere where the bulk of the observed ENA flux is generated.

- The inclusion of the internal field (case (ii)) drastically changes the ENA emission morphology compared to case (i). The spherical detector records a mostly uniform ENA flux pattern, with a slight, patch-like enhancement above the ramside apex. This patch-like feature is generated largely by parent protons that reach the upstream atmosphere along open field lines connected to the moon immediately north or south of the open-closed field line boundary. There is only a small contribution to this feature from protons on closed field lines, generated around altitudes of $1,100$–$1,200 \, \text{km}$. The portion of the detector sphere directly downstream of Ganymede records a weaker ENA flux than the surrounding locations due to absorption of parent protons by the moon (see also Cooper et al., 2001; Poppe et al., 2018).

- The reduced ENA emissions from the closed field line region also shape the synthetic images generated for case (ii): any detectors that view the region of closed field lines "side-on" display gaps in ENA flux near Ganymede's equator. In con-

trast, detectors above Ganymede's poles record an approximately uniform ring of elevated ENA flux around the moon's disc. This is because any LOS extended from these detectors through closed field lines also passes through a region of open field lines.

- The inclusion of draped electromagnetic fields (case (iii)) introduces minor changes to the ENA emission pattern found for case (ii). The enhanced magnetic field strength $|\mathbf{B}|$ in Ganymede's ramside pileup region decreases proton accessibility to the atmosphere above the moon's upstream apex. For this reason, the ENA flux through the detector sphere immediately above that region is lowered with respect to its surroundings. Synthetic ENA images captured by detectors that can view the upstream pileup region "side-on" record a substantially reduced ENA flux compared to detectors that cannot. Therefore, the field perturbations from Ganymede's interaction with the thermal Jovian plasma are most "visible" in ENA images captured by detectors that have pixels facing the pileup region.

- Between proton energies of $10\,\text{keV}$ and $100\,\text{keV}$, the hydrogen ENA flux directed from the atmosphere onto Ganymede's surface substantially exceeds the ENA flux generated at the surface by sputtering and backscattering (Pontoni et al., 2022; Szabo et al., 2024). That is, the moon's surface does not serve as a source, but rather a *sink* for ENA flux in this energy range.

- At ENA energies from $10\,\text{keV}$ to $100\,\text{keV}$, the ENA flux emitted outward from Ganymede's atmosphere surpasses the flux released from its surface by at least an order of magnitude. Hence, for most of the energy range covered by the JENI detector ($0.5-300\,\text{keV}$ for hydrogen; see Galli et al., 2022), Ganymede's atmosphere is expected to be the primary source of observable ENA emissions. A detector's ability to capture discernible ENA fluxes from the surface would depend strongly on the viewing geometry.

- The "bulge" of elevated H_2O density above Ganymede's subsolar apex does not leave a discernible signature in ENA images of the moon's mini-magnetosphere.

Our study considers Ganymede's electromagnetic environment for the conditions during the Juno PJ34 flyby, which occurred when the moon was near the center of the Jovian plasma sheet (Hansen et al., 2022). The JUICE spacecraft will sample Ganymede's environment over an extended duration (e.g., Grasset et al., 2013). Thus, a natural next step for our work is to compare modeled ENA emission patterns from Ganymede's at-

1300   mosphere at different distances between the moon and Jupiter's plasma sheet. In addi-

1301   tion, a time-dependent model for the electromagnetic fields could be applied to study

1302   the influence of reconnection on the ENA emission morphology at Ganymede.

Appendix A   Impact of the Water Vapor in Ganymede's Atmosphere on Synthetic ENA Images

1305   Synthetic ENA images in uniform electromagnetic fields (case(i)) with and with-

1306   out the atmospheric H_2O component included are displayed in Figure A1 in the left and

1307   right subplots, respectively. That is, the left subplots of Figure A1 are identical to the

1308   left subplots in Figure 9. The synthetic ENA images are organized and formatted in an

1309   identical manner manner as those in Figure 9. The results in Figures 9, 12, and A1 were

1310   generated with the same timestep. Figure A1 demonstrates that the ENA images cal-

1311   culated with and without the H_2O are indistinguishable.
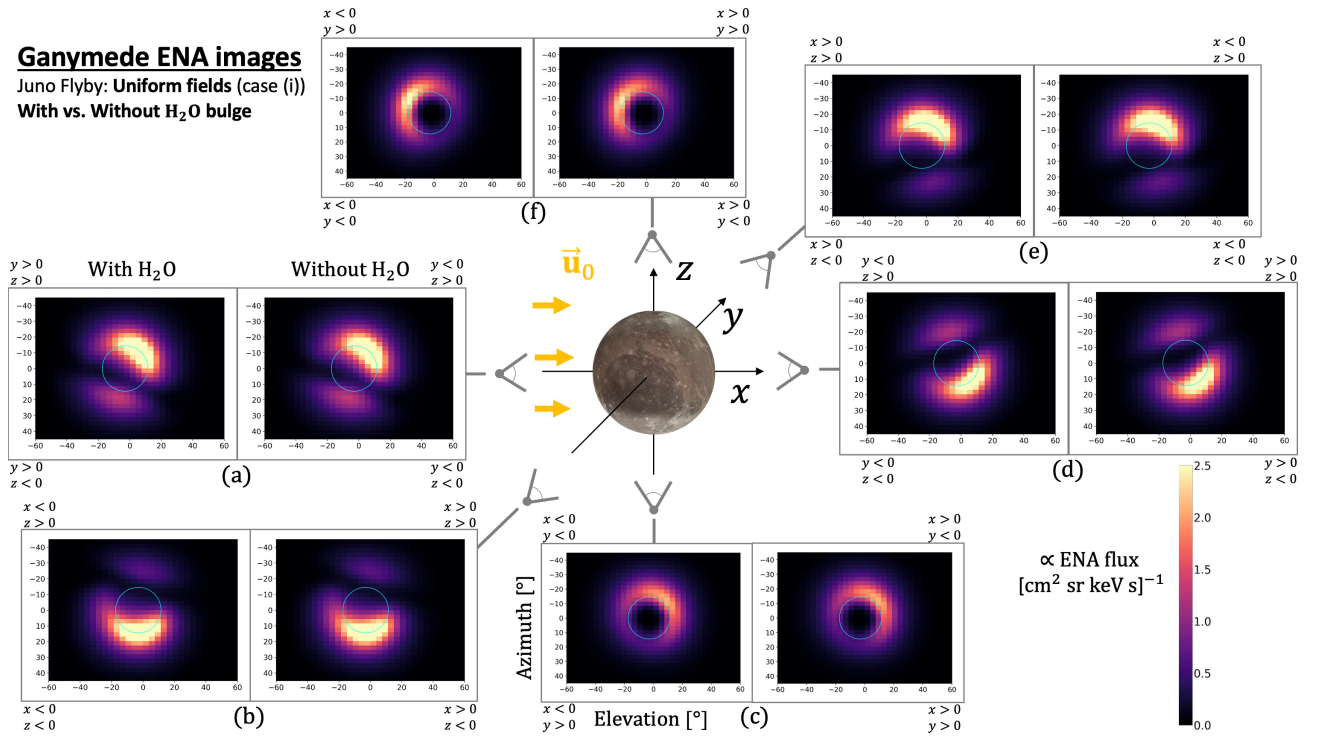
Figure A1.   Synthetic ENA images of Ganymede's magnetosphere-atmosphere interaction in uniform fields (case (i)), with (left) and without (right) the presence of the H_2O atmospheric component. The figure is arranged in the same way as Figures 9 and 12.

Acknowledgments

Open Research Section

Data supporting the production and conclusions of this work can be obtained from Haynes, Simon, and Liuzzo (2025). The electromagnetic field data from AIKEF used in this study can be found in Stahl et al. (2023).

References

Addison, P., Liuzzo, L., Arnold, H., & Simon, S. (2021). Influence of Europa's Time-Varying Electromagnetic Environment on Magnetospheric Ion Precipitation and Surface Weathering. *Journal of Geophysical Research: Space Physics*, *126*(5), e2020JA029087. Retrieved from https://agupubs.onlinelibrary.wiley.com/doi/abs/10.1029/2020JA029087 (e2020JA029087 2020JA029087) doi: https://doi.org/10.1029/2020JA029087

Alday, J., Roth, L., Ivchenko, N., Retherford, K. D., Becker, T. M., Molyneux, P., & Saur, J. (2017). New constraints on Ganymede's hydrogen corona: Analysis of Lyman-alpha emissions observed by HST/STIS between 1998 and 2014. *Planetary and Space Science*, *148*, 35-44. doi: https://doi.org/10.1016/j.pss.2017.10.006

Allegrini, F., Bagenal, F., Ebert, R., Louarn, P., Mccomas, D., Szalay, J., ... Waite, J. (2022, 07). Plasma observations during the June 7, 2021 Ganymede flyby from the Jovian Auroral Distributions Experiment (JADE) on Juno. *Geophysical Research Letters*. doi: 10.1029/2022GL098682

Allegrini, F., Gladstone, R., Hue, V., Clark, G., Szalay, J. R., Kurth, W., ... Wilson, R. J. (2020). First report of electron measurements during a Europa footprint tail crossing by Juno. *Geophysical Research Letters*, *n/a*(n/a), e2020GL089732. Retrieved from https://agupubs.onlinelibrary.wiley.com/doi/abs/10.1029/2020GL089732 doi: 10.1029/2020GL089732

Anderson, J. D., Lau, E. L., Sjogren, W. L., Schubert, G., & Moore, W. B. (1996, 12). Gravitational constraints on the internal structure of Ganymede. *Nature*, *384*(6609), 541–543. doi: 10.1038/384541a0

Bagenal, F., & Delamere, P. A. (2011). Flow of mass and energy in the magnetospheres of Jupiter and Saturn. *Journal of Geophysical Research (Space Physics)*, *116*(A5), A05209. doi: 10.1029/2010JA016294

Bagenal, F., Wilson, R. J., Siler, S., Paterson, W. R., & Kurth, W. S. (2016). Survey of Galileo plasma observations in Jupiter's plasma sheet. *Journal of Geophysical Research: Planets*, *121*(5), 871-894. Retrieved from https://agupubs.onlinelibrary.wiley.com/doi/abs/10.1002/2016JE005009 doi: https://doi.org/10.1002/2016JE005009

Barth, C. A., Hord, C. W., Stewart, A. I. F., Pryor, W. R., Simmons, K. E., Mc-

Clintock, W. E., ... Aiello, J. J. (1997). Galileo ultraviolet spectrometer observations of atomic hydrogen in the atmosphere of Ganymede. *Geophysical Research Letters*, *24*(17), 2147-2150. Retrieved from `https://agupubs.onlinelibrary.wiley.com/doi/abs/10.1029/97GL01927` doi: https://doi.org/10.1029/97GL01927

Bonfond, B., Hess, S., Bagenal, F., Gérard, J.-C., Grodent, D., Radioti, A., ... Clarke, J. T. (2013). The multiple spots of the Ganymede auroral footprint. *Geophysical Research Letters*, *40*(19), 4977-4981. doi: https://doi.org/10.1002/grl.50989

Boutonnet, A., Langevin, Y., & Erd, C. (2024, September). Designing the JUICE Trajectory. *Space Science Reviews*, *220*(6), 67. doi: 10.1007/s11214-024-01093-y

Brandt, P. C., Nikoukar, R., DeMajistre, R., Allen, R. C., Mitchell, D. G., Roelof, E. C., ... Parker, C. W. (2022). Energetic Neutral Atom Imaging of the Terrestrial Global Magnetosphere. In Y. Colado-Vega, D. Gallagher, H. Frey, & S. Wing (Eds.), *Understanding the space environment through global measurements* (p. 23-58). Elsevier. Retrieved from `https://www.sciencedirect.com/science/article/pii/B9780128206300000076` doi: https://doi.org/10.1016/B978-0-12-820630-0.00007-6

Buccino, D. R., Parisi, M., Gramigna, E., Gomez-Casajus, L., Tortora, P., Zannoni, M., ... Bolton, S. (2022). Ganymede's Ionosphere Observed by a Dual-Frequency Radio Occultation With Juno. *Geophysical Research Letters*, *49*(23), e2022GL098420. doi: https://doi.org/10.1029/2022GL098420

Calvin, W. M., & Spencer, J. R. (1997). Latitudinal distribution of O2 on Ganymede: Observations with the Hubble Space Telescope. *Icarus*, *130*(2), 505–516. doi: 10.1006/icar.1997.5842

Carberry Mogan, S. R., Johnson, R. E., Vorburger, Audrey, & Roth, Lorenz. (2023). Electron impact ionization in the icy Galilean satellites´ atmospheres. *Eur. Phys. J. D*, *77*(2), 26. Retrieved from `https://doi.org/10.1140/epjd/s10053-023-00606-8` doi: 10.1140/epjd/s10053-023-00606-8

Carnielli, G., Galand, M., Leblanc, F., Leclercq, L., Modolo, R., Beth, A., ... Jia, X. (2019). First 3D test particle model of Ganymede's ionosphere. *Icarus*, *330*(October 2017), 42–59. doi: 10.1016/j.icarus.2019.04.016

Carnielli, G., Galand, M., Leblanc, F., Modolo, R., Beth, A., & Jia, X. (2020). Simulations of ion sputtering at Ganymede. *Icarus*, *351*, 113918. doi: https://doi.org/10.1016/j.icarus.2020.113918

Clark, G., Kollmann, P., Mauk, B. H., Paranicas, C., Haggerty, D., Rymer, A., ... Turner, D. L. (2022). Energetic Charged Particle Observations During Juno's Close Flyby of Ganymede. *Geophysical Research Letters*, *49*(23), e2022GL098572. Retrieved from https://agupubs.onlinelibrary.wiley.com/doi/abs/10.1029/2022GL098572 (e2022GL098572 2022GL098572) doi: https://doi.org/10.1029/2022GL098572

Clark, G., Mauk, B., Paranicas, C., Haggerty, D. K., Kollmann, P., Rymer, A. M., ... Szalay, J. R. (2019, December). Energetic particle observations in Jupiter's polar magnetosphere: new discoveries by Juno. In *Agu fall meeting abstracts* (Vol. 2019, p. P42A-01).

Clark, G., Mauk, B. H., Kollmann, P., Paranicas, C., Bagenal, F., Allen, R. C., ... Westlake, J. H. (2020). Heavy Ion Charge States in Jupiter's Polar Magnetosphere Inferred From Auroral Megavolt Electric Potentials. *Journal of Geophysical Research: Space Physics*, *125*(9), e2020JA028052. Retrieved from https://agupubs.onlinelibrary.wiley.com/doi/abs/10.1029/2020JA028052 (e2020JA028052 2020JA028052) doi: https://doi.org/10.1029/2020JA028052

Clark, G., Mauk, B. H., Paranicas, C., Kollmann, P., & Smith, H. T. (2016, March). Charge states of energetic oxygen and sulfur ions in Jupiter's magnetosphere. *Journal of Geophysical Research (Space Physics)*, *121*, 2264-2273. doi: 10.1002/2015JA022257

Cooper, J. F., Johnson, R. E., Mauk, B. H., Garrett, H. B., & Gehrels, N. (2001). Energetic ion and electron irradiation of the icy Galilean satellites. *Icarus*, *149*(1), 133–159. doi: 10.1006/icar.2000.6498

Devinat, M., Blanc, M., & André, N. (2024). A Self-Consistent Model of Radial Transport in the Magnetodisks of Gas Giants Including Interhemispheric Asymmetries. *Journal of Geophysical Research: Space Physics*, *129*(4), e2023JA032233. Retrieved from https://agupubs.onlinelibrary.wiley.com/doi/abs/10.1029/2023JA032233 (e2023JA032233 2023JA032233) doi: https://doi.org/10.1029/2023JA032233

Dialynas, K., Krimigis, S. M., Mitchell, D. G., Roelof, E. C., & Decker, R. B. (2013, nov). A Three-Coordinate System (Ecliptic, Galactic, ISMF) Spectral Analysis of Heliospheric ENA Emissions using Cassini/INCA Measurements. *The Astrophysical Journal*, *778*(1), 40. Retrieved from `https://dx.doi.org/10.1088/0004-637X/778/1/40` doi: 10.1088/0004-637X/778/1/40

Duling, S., Saur, J., Clark, G., Allegrini, F., Greathouse, T., Gladstone, R., . . . Sulaiman, A. H. (2022). Ganymede MHD Model: Magnetospheric Context for Juno's PJ34 Flyby. *Geophysical Research Letters*, *49*(24). doi: https://doi.org/10.1029/2022GL101688

Duling, S., Saur, J., & Wicht, J. (2014). Consistent boundary conditions at nonconducting surfaces of planetary bodies: Applications in a new Ganymede MHD model. *Journal of Geophysical Research: Space Physics*, *119*(6), 4412–4440. doi: 10.1002/2013JA019554

Ebert, R. W., Fuselier, S. A., Allegrini, F., Bagenal, F., Bolton, S. J., Clark, G., . . . Wilson, R. J. (2022). Evidence for Magnetic Reconnection at Ganymede's Upstream Magnetopause During the PJ34 Juno Flyby. *Geophysical Research Letters*, *49*(23). doi: https://doi.org/10.1029/2022GL099775

Eviatar, A., Strobel, D. F., Wolven, B. C., Feldman, P. D., McGrath, M. A., & Williams, D. J. (2001, 7). Excitation of the Ganymede ultraviolet aurora. *The Astrophysical Journal*, *555*(2), 1013. doi: 10.1086/321510

Eviatar, A., Williams, D. J., Paranicas, C., McEntire, R. W., Mauk, B. H., & Kivelson, M. G. (2000). Trapped Energetic Electrons in the Magnetosphere of Ganymede. *Journal of Geophysical Research: Space Physics*, *105*(A3), 5547–5553. doi: 10.1029/1999ja900450

Fatemi, S., Poppe, A., Khurana, K., Holmström, M., & Delory, G. (2016). On the formation of Ganymede's surface brightness asymmetries: Kinetic simulations of Ganymede's magnetosphere. *Geophysical Research Letters*, *43*(10), 4745–4754. doi: 10.1002/2016GL068363

Fatemi, S., Poppe, A. R., Vorburger, A., Lindkvist, J., & Hamrin, M. (2022). Ion Dynamics at the Magnetopause of Ganymede. *Journal of Geophysical Research: Space Physics*, *127*(1). Retrieved from `https://agupubs.onlinelibrary.wiley.com/doi/abs/10.1029/2021JA029863` doi: https://doi.org/10.1029/2021JA029863

Feldman, P. D., McGrath, M. A., Strobel, D. F., Moos, H. W., Retherford, K. D., & Wolven, B. C.   (2000, 6).   HST/STIS ultraviolet imaging of polar aurora on Ganymede.   *The Astrophysical Journal*, *535*(2), 1085–1090.   doi: 10.1086/308889

Galli, A., Vorburger, A., Carberry Mogan, S. R., Roussos, E., Stenberg Wieser, G., Wurz, P., ... Liuzzo, L.   (2022).   Callisto's Atmosphere and Its Space Environment: Prospects for the Particle Environment Package on Board JUICE.   *Earth and Space Science*, *9*(5), e2021EA002172.   Retrieved from `https://agupubs.onlinelibrary.wiley.com/doi/abs/10.1029/2021EA002172` (e2021EA002172 2021EA002172) doi: https://doi.org/10.1029/2021EA002172

Galli, A., Vorburger, A., Wurz, P., Galand, M., Oza, A., Fatemi, S., ... Mura, A. (2025).   Interactions between the Space Environment and Ganymede's Surface. In *Ganymede* (p. 237–251). Cambridge University Press.

Grasset, O., Dougherty, M., Coustenis, A., Bunce, E., Erd, C., Titov, D., ... Van Hoolst, T.   (2013).   JUpiter ICy moons Explorer (JUICE): An ESA mission to orbit Ganymede and to characterise the Jupiter system.   *Planetary and Space Science*, *78*, 1-21.   Retrieved from `https://www.sciencedirect.com/science/article/pii/S0032063312003777`   doi: https://doi.org/10.1016/j.pss.2012.12.002

Gurnett, D. A., Kurth, W. S., Roux, A., Bolton, S. J., & Kennel, C. F.   (1996, 12). Evidence for a magnetosphere at Ganymede from plasma-wave observations by the Galileo spacecraft. *Nature*, *384*(6609), 535–537. doi: 10.1038/384535a0

Hall, D. T., Feldman, P. D., McGrath, M. A., & Strobel, D. F.   (1998, may).   The Far-Ultraviolet Oxygen Airglow of Europa and Ganymede.   *The Astrophysical Journal*, *499*(1), 475.   Retrieved from `https://dx.doi.org/10.1086/305604` doi: 10.1086/305604

Hansen, C. J., Bolton, S., Sulaiman, A. H., Duling, S., Bagenal, F., Brennan, M., ... Withers, P.   (2022).   Juno's Close Encounter With Ganymede-An Overview. *Geophysical Research Letters*, *49*(23). doi: https://doi.org/10.1029/2022GL099285

Hansen, G. B., & McCord, T. B.   (2004).   Amorphous and crystalline ice on the Galilean satellites: A balance between thermal and radiolytic processes.   *Journal of Geophysical Research*, *109*(E1), E01012. doi: 10.1029/2003JE002149

Haynes, C. M., Simon, S., & Liuzzo, L. (2025). Data for "Emission of Energetic Neutral Atoms from Ganymede's Magnetosphere-Atmosphere Interaction" by Haynes et al., 2025 [Data set]. *Zenodo*, https://doi.org/10.5281/zenodo.15855582. doi: 10.5281/zenodo.15855582

Haynes, C. M., Tippens, T., Addison, P., Liuzzo, L., Poppe, A. R., & Simon, S. (2023). Emission of Energetic Neutral Atoms from the Magnetosphere-Atmosphere Interactions at Callisto and Europa. *Journal of Geophysical Research: Space Physics*, *128*, e2023JA031931. doi: 10.1029/2023JA031931

Haynes, C. M., Tippens, T., Simon, S., & Liuzzo, L. (2025). Constraints on the Observability of Energetic Neutral Atoms From the Magnetosphere-Atmosphere Interactions at Callisto and Europa. *Journal of Geophysical Research: Space Physics*, *130*(1), e2024JA033391. Retrieved from `https://agupubs.onlinelibrary.wiley.com/doi/abs/10.1029/2024JA033391` (e2024JA033391 2024JA033391) doi: https://doi.org/10.1029/2024JA033391

Hue, V., Gladstone, G. R., Louis, C. K., Greathouse, T. K., Bonfond, B., Szalay, J. R., . . . Connerney, J. E. P. (2023). The Io, Europa, and Ganymede Auroral Footprints at Jupiter in the Ultraviolet: Positions and Equatorial Lead Angles. *Journal of Geophysical Research: Space Physics*, *128*(5), e2023JA031363. Retrieved from `https://agupubs.onlinelibrary.wiley.com/doi/abs/10.1029/2023JA031363` (e2023JA031363 2023JA031363) doi: https://doi.org/10.1029/2023JA031363

Ip, W.-H. H., Williams, D. J., McEntire, R. W., & Mauk, B. (1997). Energetic ion sputtering effects at Ganymede. *Geophysical Research Letters*, *24*(21), 2631–2634. doi: 10.1029/97GL02814

Jia, X., & Kivelson, M. G. (2021). The Magnetosphere of Ganymede. In *Magnetospheres in the solar system* (p. 557-573). American Geophysical Union (AGU). Retrieved from `https://agupubs.onlinelibrary.wiley.com/doi/abs/10.1002/9781119815624.ch35` doi: https://doi.org/10.1002/9781119815624.ch35

Jia, X., Kivelson, M. G., Khurana, K. K., & Walker, R. J. (2025). Improved Models of Ganymede's Permanent and Induced Magnetic Fields Based on Galileo and Juno Data. *Journal of Geophysical Research: Planets*, *130*(1), e2024JE008309. Retrieved from `https://agupubs.onlinelibrary.wiley.com/doi/abs/`

10.1029/2024JE008309 (e2024JE008309 2024JE008309) doi: https://doi.org/
10.1029/2024JE008309

Jia, X., Walker, R. J., Kivelson, M. G., Khurana, K. K., & Linker, J. A.   (2008, 6).
Three-dimensional MHD simulations of Ganymede's magnetosphere. *Journal of Geophysical Research: Space Physics*, *113*(6). doi: 10.1029/2007JA012748

Jia, X., Walker, R. J., Kivelson, M. G., Khurana, K. K., & Linker, J. A.   (2009).
Properties of Ganymede's magnetosphere inferred from improved three-dimensional MHD simulations.   *Journal of Geophysical Research: Space Physics*, *114*(9). doi: 10.1029/2009JA014375

Jia, X., Walker, R. J., Kivelson, M. G., Khurana, K. K., & Linker, J. A. (2010). Dynamics of Ganymede's magnetopause: Intermittent reconnection under steady external conditions.   *Journal of Geophysical Research: Space Physics*, *115*(12). doi: 10.1029/2010JA015771

Johnson, R. E.   (1990).   *Energetic Charged-Particle Interactions with Atmospheres and Surfaces.* doi: 10.1007/978-3-642-48375-2

Johnson, R. E., Carlson, R., Cooper, J., Paranicas, C., Moore, M., & Wong, M.
(2004). Radiation effects on the surfaces of the Galilean satellites. *Jupiter. The Planet, satellites and magnetosphere.*, *51*(7), 483–510.

Johnson, R. E., Lanzerotti, L. J., Brown, W. L., & Armstrong, T. P.   (1981).   Erosion of Galilean Satellite Surfaces by Jovian Magnetosphere Particles.   *Science*, *212*(4498), 1027-1030. Retrieved from https://www.science.org/doi/abs/10.1126/science.212.4498.1027   doi: 10.1126/science.212.4498.1027

Johnson, R. E., & Quickenden, T.   (1997).   Photolysis and radiolysis of water ice on outer solar system bodies.   *Journal of Geophysical Research E: Planets*, *102*(E5), 10985–10996. doi: 10.1029/97JE00068

Joseph, J., Kurth, W. S., Sulaiman, A. H., Connerney, J. E. P., Allegrini, F.,
Duling, S., . . . Bolton, S. J.   (2024).   Evidence of Magnetic Reconnection in Ganymede's Wake Region From Juno.   *Journal of Geophysical Research: Space Physics*, *129*(12), e2024JA033173.   Retrieved from https://agupubs.onlinelibrary.wiley.com/doi/abs/10.1029/2024JA033173 (e2024JA033173 2024JA033173) doi: https://doi.org/10.1029/2024JA033173

Joy, S. P., Kivelson, M. G., Walker, R. J., Khurana, K. K., Russell, C. T., & Ogino,
T. (2002, 10). Probabilistic models of the Jovian magnetopause and bow shock

locations. *Journal of Geophysical Research (Space Physics)*, *107*(A10), 1309. doi: 10.1029/2001JA009146

Khurana, K. K., Pappalardo, R. T., Murphy, N., & Denk, T. (2007). The origin of Ganymede's polar caps. *Icarus*, *191*(1), 193-202. Retrieved from `https://www.sciencedirect.com/science/article/pii/S0019103507001935` doi: https://doi.org/10.1016/j.icarus.2007.04.022

Kim, T. K., Ebert, R. W., Valek, P. W., Allegrini, F., McComas, D. J., Bagenal, F., ... Bolton, S. J. (2020). Survey of Ion Properties in Jupiter's Plasma Sheet: Juno JADE-I Observations. *Journal of Geophysical Research: Space Physics*, *125*(4), e2019JA027696. doi: https://doi.org/10.1029/2019JA027696

Kivelson, M., Khurana, K. K., Russell, C. T., Walker, R. J., Warnecke, J., Coroniti, F. V., ... Schubert, G. (1996). Discovery of Ganymede's magnetic field by the Galileo spacecraft. *Nature*, *384*(6609), 537–541. doi: 10.1038/384537a0

Kivelson, M. G., Bagenal, F., Jia, X., & Khurana, K. K. (2025). Ganymede: Its Magnetosphere and Its Interaction with the Jovian Magnetosphere. In *Ganymede* (p. 215–236). Cambridge University Press.

Kivelson, M. G., Bagenal, F., Kurth, W. S., Neubauer, F. M., Paranicas, C., & Saur, J. (2004). Magnetospheric interactions with satellites. In F. Bagenal, T.E. Dowling and W.B. McKinnon (Ed.), *Jupiter. The planet, satellites and magnetosphere* (pp. 513–536). Cambridge Univ. Press.

Kivelson, M. G., Khurana, K. K., & Volwerk, M. (2002, 6). The permanent and inductive magnetic moments of Ganymede. *Icarus*, *157*(2), 507–522. doi: 10.1006/icar.2002.6834

Kliore, A. J. (1998). Satellite Atmospheres and Magnetospheres. In J. Andersen (Ed.), *Highlights of astronomy: As presented at the xxiiird general assembly of the iau, 1997* (pp. 1065–1069). Dordrecht: Springer Netherlands. doi: 10.1007/978-94-011-4778-1_138

Kollmann, P., Clark, G., Paranicas, C., Mauk, B., Haggerty, D., Rymer, A., & Allegrini, F. (2022). Ganymede's Radiation Cavity and Radiation Belts. *Geophysical Research Letters*, *49*(23), e2022GL098474. Retrieved from `https://agupubs.onlinelibrary.wiley.com/doi/abs/10.1029/2022GL098474` (e2022GL098474 2022GL098474) doi: https://doi.org/10.1029/2022GL098474

Krimigis, S. M., Mitchell, D. G., Hamilton, D. C., Livi, S., Dandouras, J., Jaskulek,

S., ... Williams, D. J. (2004, September). Magnetosphere Imaging Instrument (MIMI) on the Cassini Mission to Saturn/Titan. *Space Science Reviews*, *114*, 233–329, doi: 10.1007/s11214-004-1410-8.

Kurth, W., Sulaiman, A., Hospodarsky, G., Mauk, J., & Clark, G. (2022). Juno Plasma Wave Observations at Ganymede. *Geophysical Research Letters*, *n/a*(n/a). doi: https://doi.org/10.1029/2022GL098591

Leblanc, F., Oza, A. V., Leclercq, L., Schmidt, C., Cassidy, T., Modolo, R., ... Johnson, R. E. (2017, 9). On the orbital variability of Ganymede's atmosphere. *Icarus*, *293*, 185–198. doi: 10.1016/j.icarus.2017.04.025

Leblanc, F., Roth, L., Chaufray, J., Modolo, R., Galand, M., Ivchenko, N., ... Werner, A. (2023). Ganymede's atmosphere as constrained by HST/STIS observations. *Icarus*, 115557. doi: https://doi.org/10.1016/j.icarus.2023.115557

Ligier, N., Paranicas, C., Carter, J., Poulet, F., Calvin, W., Nordheim, T., ... Ferellec, L. (2019). Surface composition and properties of ganymede: Updates from ground-based observations with the near-infrared imaging spectrometer sinfoni/vlt/eso. *Icarus*, *333*, 496-515. Retrieved from `https://www.sciencedirect.com/science/article/pii/S0019103519300053` doi: https://doi.org/10.1016/j.icarus.2019.06.013

Lindsay, B. G., & Stebbings, R. F. (2005, December). Charge transfer cross sections for energetic neutral atom data analysis. *Journal of Geophysical Research (Space Physics)*, *110*(A9), A12213. doi: 10.1029/2005JA011298

Liuzzo, L., Nénon, Q., Poppe, A. R., Stahl, A., Simon, S., & Fatemi, S. (2024). On the Formation of Trapped Electron Radiation Belts at Ganymede. *Geophysical Research Letters*, *51*(10), e2024GL109058. Retrieved from `https://agupubs.onlinelibrary.wiley.com/doi/abs/10.1029/2024GL109058` (e2024GL109058 2024GL109058) doi: https://doi.org/10.1029/2024GL109058

Liuzzo, L., Poppe, A. R., Addison, P., Simon, S., Nénon, Q., & Paranicas, C. (2022). Energetic Magnetospheric Particle Fluxes onto Callisto's Atmosphere. *Journal of Geophysical Research: Space Physics*, *n/a*(n/a), e2022JA030915. Retrieved from `https://agupubs.onlinelibrary.wiley.com/doi/abs/10.1029/2022JA030915` (e2022JA030915 2022JA030915) doi: https://doi.org/10.1029/2022JA030915

Liuzzo, L., Poppe, A. R., Paranicas, C., Nénon, Q., Fatemi, S., & Simon, S. (2020).

Variability in the Energetic Electron Bombardment of Ganymede. *Journal of Geophysical Research: Space Physics*, *125*(9), e2020JA028347. Retrieved from `https://agupubs.onlinelibrary.wiley.com/doi/abs/10.1029/2020JA028347` (e2020JA028347 10.1029/2020JA028347) doi: https://doi.org/10.1029/2020JA028347

Liuzzo, L., Simon, S., & Regoli, L. (2019). Energetic ion dynamics near Callisto. *Planetary and Space Science*, *166*, 23-53. Retrieved from `https://www.sciencedirect.com/science/article/pii/S0032063318301648` doi: https://doi.org/10.1016/j.pss.2018.07.014

Loand, H., & Tite, W. (1969). Electron-capture and loss cross sections for fast, heavy particles passing through gases. *Atomic Data and Nuclear Data Tables*, *1*, 305-328. Retrieved from `https://www.sciencedirect.com/science/article/pii/S0092640X69800252` doi: https://doi.org/10.1016/S0092-640X(69)80025-2

Marconi, M. L. (2007, 9). A kinetic model of Ganymede's atmosphere. *Icarus*, *190*(1), 155–174. doi: 10.1016/j.icarus.2007.02.016

Massey, H. S. W., Burhop, E. H. S., & McDaniel, E. (1970). Electronic and Ionic Impact Phenomena. *American Journal of Physics*, *38*(4), 551–551.

Mauk, B. H., Haggerty, D. K., Jaskulek, S. E., Schlemm, C. E., Brown, L. E., Cooper, S. A., . . . Stokes, M. R. (2017). The Jupiter Energetic Particle Detector Instrument (JEDI) Investigation for the Juno Mission. *Space Science Reviews*, *213*, 289-346.

Mauk, B. H., Mitchell, D., McEntire, R., Paranicas, C., Roelof, E., Williams, D., . . . Lagg, A. (2004). Energetic ion characteristics and neutral gas interactions in Jupiter's magnetosphere. *Journal of Geophysical Research: Space Physics*, *109*(A9). doi: 10.1029/2003JA010270

McComas, D. J., Alexander, N., Allegrini, F., Bagenal, F., Beebe, C. R., Clark, G., . . . White, D. (2017). The Jovian Auroral Distributions Experiment (JADE) on the Juno Mission to Jupiter. *Space Science Reviews*, *213*, 547-643.

Mitchell, D. G., Brandt, P. C., Roelof, E. C., Dandouras, J., Krimigis, S. M., & Mauk, B. H. (2005). Energetic Neutral Atom Emissions from Titan Interaction with Saturn's Magnetosphere. *Science*, *308*(5724), 989-992. Retrieved from `https://www.science.org/doi/abs/10.1126/science.1109805` doi:

10.1126/science.1109805

Mitchell, D. G., Brandt, P. C., Westlake, J. H., Jaskulek, S. E., Andrews, G. B., & Nelson, K. S. (2016). Energetic particle imaging: The evolution of techniques in imaging high-energy neutral atom emissions. *Journal of Geophysical Research: Space Physics*, *121*(9), 8804-8820. Retrieved from `https://agupubs.onlinelibrary.wiley.com/doi/abs/10.1002/2016JA022586` doi: https://doi.org/10.1002/2016JA022586

Mitchell, D. G., Cheng, A. F., Krimigis, S. M., Keath, E. P., Jaskulek, S. E., Mauk, B. H., . . . Drake, V. A. (1993). INCA: the ion neutral camera for energetic neutral atom imaging of the Saturnian magnetosphere. *Optical Engineering*, *32*(12), 3096 – 3101. Retrieved from `https://doi.org/10.1117/12.155609` doi: 10.1117/12.155609

Müller, J., Simon, S., Motschmann, U., Schüle, J., Glassmeier, K.-H., & Pringle, G. J. (2011). A.I.K.E.F.: Adaptive hybrid model for space plasma simulations. *Computer Physics Communications*, *182*(4), 946-966. Retrieved from `https://www.sciencedirect.com/science/article/pii/S0010465510005266` doi: https://doi.org/10.1016/j.cpc.2010.12.033

Neubauer, F. M. (1980). Nonlinear standing Alfven wave current system at Io - Theory. *J. Geophys. Res.*, *85*, 1171–1178. doi: 10.1029/JA085iA03p01171

Neubauer, F. M. (1998). The sub-Alfvénic interaction of the Galilean satellites with the Jovian magnetosphere. *J. Geophys. Res.*, *103*, 19843–19866. doi: 10.1029/97JE03370

Nordheim, T. A., Regoli, L. H., Harris, C. D. K., Paranicas, C., Hand, K. P., & Jia, X. (2022, jan). Magnetospheric Ion Bombardment of Europa's Surface. *The Planetary Science Journal*, *3*(1), 5. Retrieved from `https://dx.doi.org/10.3847/PSJ/ac382a` doi: 10.3847/PSJ/ac382a

Nénon, Q., & André, N. (2019). Evidence of Europa Neutral Gas Torii From Energetic Sulfur Ion Measurements. *Geophysical Research Letters*, *46*(7), 3599-3606. Retrieved from `https://agupubs.onlinelibrary.wiley.com/doi/abs/10.1029/2019GL082200` doi: https://doi.org/10.1029/2019GL082200

Ogasawara, K., Dayeh, M. A., Fuselier, S. A., Goldstein, J., McComas, D. J., & Valek, P. (2019). Terrestrial Energetic Neutral Atom Emissions and the Ground-Based Geomagnetic Indices: Implications From IBEX Observations.

Journal of Geophysical Research: Space Physics, *124*(11), 8761-8777. Retrieved from https://agupubs.onlinelibrary.wiley.com/doi/abs/10.1029/2019JA026976 doi: https://doi.org/10.1029/2019JA026976

Paranicas, C., Mauk, B. H., Kollmann, P., Clark, G., Haggerty, D. K., Westlake, J., ... Bolton, S. (2022). Energetic Charged Particle Fluxes Relevant to Ganymede's Polar Region. *Geophysical Research Letters*, *49*(23), e2022GL098077. Retrieved from https://agupubs.onlinelibrary.wiley.com/doi/abs/10.1029/2022GL098077 (e2022GL098077 2022GL098077) doi: https://doi.org/10.1029/2022GL098077

Paranicas, C., Paterson, W. R., Cheng, A. F., Mauk, B. H., McEntire, R. W., Frank, L. A., & Williams, D. J. (1999). Energetic particle observations near Ganymede. *Journal of Geophysical Research: Space Physics*, *104*(A8), 17459-17469. Retrieved from https://agupubs.onlinelibrary.wiley.com/doi/abs/10.1029/1999JA900199 doi: https://doi.org/10.1029/1999JA900199

Paranicas, C., Szalay, J. R., Mauk, B. H., Clark, G., Kollmann, P., Haggerty, D. K., ... Bolton, S. (2021). Energy Spectra Near Ganymede From Juno Data. *Geophysical Research Letters*, *48*(10), e2021GL093021. Retrieved from https://agupubs.onlinelibrary.wiley.com/doi/abs/10.1029/2021GL093021 (e2021GL093021 2021GL093021) doi: https://doi.org/10.1029/2021GL093021

Paty, C., Paterson, W., & Winglee, R. (2008, June). Ion energization in Ganymede's magnetosphere: Using multifluid simulations to interpret ion energy spectrograms. *Journal of Geophysical Research (Space Physics)*, *113*, A06211. doi: 10.1029/2007JA012848

Paty, C., & Winglee, R. (2004). Multi-fluid simulations of Ganymede's magnetosphere. *Geophys. Res. Lett.*, *31*, L24806 (1–5), doi:10.1029/2004GL021220.

Payan, A. P., Paty, C. S., & Retherford, K. D. (2015). Uncovering local magnetospheric processes governing the morphology and variability of Ganymede's aurora using three-dimensional multifluid simulations of Ganymede's magnetosphere. *Journal of Geophysical Research: Space Physics*, *120*(1), 401–413. doi: 10.1002/2014JA020301

Plainaki, C., Massetti, S., Jia, X., Mura, A., Milillo, A., Grassi, D., ... Filacchione, G. (2020, sep). Kinetic Simulations of the Jovian Energetic Ion Circulation around Ganymede. *The Astrophysical Journal*, *900*(1), 74.

Retrieved from https://dx.doi.org/10.3847/1538-4357/aba94c   doi: 10.3847/1538-4357/aba94c

Plainaki, C., Massetti, S., Jia, X., Mura, A., Roussos, E., Milillo, A., & Grassi, D. (2022, dec).   The Jovian Energetic Ion Environment of Ganymede: Planetary Space Weather Considerations in View of the JUICE Mission.   *The Astrophysical Journal*, *940*(2), 186.   Retrieved from https://dx.doi.org/10.3847/1538-4357/ac9c54 doi: 10.3847/1538-4357/ac9c54

Plainaki, C., Milillo, A., Massetti, S., Mura, A., Jia, X., Orsini, S., . . . Rispoli, R. (2015).   The H2O and O2 exospheres of Ganymede: The result of a complex interaction between the Jovian magnetospheric ions and the icy moon. *Icarus*, *245*, 306-319.   Retrieved from https://www.sciencedirect.com/science/article/pii/S0019103514004801   doi: https://doi.org/10.1016/j.icarus.2014.09.018

Plainaki, C., Milillo, A., Mura, A., Orsini, S., & Cassidy, T.   (2010).   Neutral particle release from Europa's surface.   *Icarus*, *210*(1), 385-395.   Retrieved from https://www.sciencedirect.com/science/article/pii/S0019103510002691 doi: https://doi.org/10.1016/j.icarus.2010.06.041

Plainaki, C., Milillo, A., Mura, A., Orsini, S., Massetti, S., & Cassidy, T.   (2012, 4). The role of sputtering and radiolysis in the generation of Europa exosphere. *Icarus*, *218*(2), 956–966. doi: 10.1016/j.icarus.2012.01.023

Pontoni, A., Shimoyama, M., Futaana, Y., Fatemi, S., Poppe, A. R., Wieser, M., & Barabash, S. (2022). Simulations of Energetic Neutral Atom Sputtering From Ganymede in Preparation for the JUICE Mission.   *Journal of Geophysical Research: Space Physics*, *127*(1), e2021JA029439.   Retrieved from https://agupubs.onlinelibrary.wiley.com/doi/abs/10.1029/2021JA029439 (e2021JA029439 2021JA029439) doi: https://doi.org/10.1029/2021JA029439

Poppe, A. R., Fatemi, S., & Khurana, K. K.   (2018). Thermal and energetic ion dynamics in Ganymede's magnetosphere. *Journal of Geophysical Research (Space Physics)*, *123*, 4614–4637. doi: 10.1029/2018JA025312

Roelof, E. C.   (1987).   Energetic neutral atom image of a storm-time ring current. *Geophysical Research Letters*, *14*(6), 652-655. Retrieved from https://agupubs.onlinelibrary.wiley.com/doi/abs/10.1029/GL014i006p00652 doi: https://doi.org/10.1029/GL014i006p00652

Romanelli, N., DiBraccio, G. A., Modolo, R., Connerney, J. E. P., Ebert, R. W., Martos, Y. M., ... Bolton, S. J. (2022). Juno Magnetometer Observations at Ganymede: Comparisons With a Global Hybrid Simulation and Indications of Magnetopause Reconnection. *Geophysical Research Letters*, *49*(23). doi: https://doi.org/10.1029/2022GL099545

Roth, L., Ivchenko, N., Gladstone, G. R., Saur, J., Grodent, D., Bonfond, B., ... Retherford, K. D. (2021, October). A sublimated water atmosphere on Ganymede detected from Hubble Space Telescope observations. *Nature Astronomy*, *5*, 1043-1051. doi: 10.1038/s41550-021-01426-9

Roth, L., Plainaki, C., Oza, A., Vorburger, A., Johnson, R. E., Molyneux, P., ... Wurz, P. (2025). Ganymede's Tenuous Atmosphere. In *Ganymede* (p. 252-268). Cambridge University Press.

Santos, A., Achilleos, N., Millas, D., Dunn, W., Guio, P., & Arridge, C. S. (2024). Characterizing the Magnetic and Plasma Environment Upstream of Ganymede. *Journal of Geophysical Research: Space Physics*, *129*(10), e2024JA032689. Retrieved from https://agupubs.onlinelibrary.wiley.com/doi/abs/10.1029/2024JA032689 (e2024JA032689 2024JA032689) doi: https://doi.org/10.1029/2024JA032689

Sarkango, Y., Szalay, J. R., Poppe, A. R., Nénon, Q., Kollmann, P., Clark, G., & McComas, D. J. (2023). Proton Equatorial Pitch Angle Distributions in Jupiter's Inner Magnetosphere. *Geophysical Research Letters*, *50*(11), e2023GL104374. Retrieved from https://agupubs.onlinelibrary.wiley.com/doi/abs/10.1029/2023GL104374 (e2023GL104374 2023GL104374) doi: https://doi.org/10.1029/2023GL104374

Saur, J., Duling, S., Roth, L., Jia, X., Strobel, D. F., Feldman, P. D., ... Hartkorn, O. (2015). The search for a subsurface ocean in Ganymede with Hubble Space Telescope observations of its auroral ovals. *Journal of Geophysical Research: Space Physics*, *120*(3), 1715-1737. Retrieved from https://agupubs.onlinelibrary.wiley.com/doi/abs/10.1002/2014JA020778 doi: https://doi.org/10.1002/2014JA020778

Schilling, N., Neubauer, F. M., & Saur, J. (2007). Time-varying interaction of Europa with the Jovian magnetosphere: Constraints on the conductivity of Europa's subsurface ocean. *Icarus*, *192*(1), 41-55. Retrieved from https://

www.sciencedirect.com/science/article/pii/S0019103507002837   doi: https://doi.org/10.1016/j.icarus.2007.06.024

Seufert, M., Saur, J., & Neubauer, F. M.   (2011).   Multi-frequency electromagnetic sounding of the Galilean moons. *Icarus*, *214*(2), 477–494. doi: 10.1016/j.icarus .2011.03.017

Shprits, Y. Y., Menietti, J. D., Drozdov, A. Y., Horne, R. B., Woodfield, E. E., Groene, J. B., ... Gurnett, D. A.   (2018).   Strong whistler mode waves observed in the vicinity of Jupiter's moons. *Nature Communications*, *9*(1), 7–12. doi: 10.1038/s41467-018-05431-x

Southwood, D. J., & Kivelson, M. G.   (1987).   Magnetospheric Interchange Instability.   *Journal of Geophysical Research: Space Physics*, *92*(A1), 109-116. Retrieved from https://agupubs.onlinelibrary.wiley.com/doi/abs/ 10.1029/JA092iA01p00109 doi: https://doi.org/10.1029/JA092iA01p00109

Spencer, J. R., Calvin, W. M., & Person, M. J. (1995). Charge-coupled device spectra of the Galilean satellites: Molecular oxygen on Ganymede. *Journal of Geophysical Research*, *100*(E9), 19049. doi: 10.1029/95JE01503

Stahl, A., Addison, P., Simon, S., & Liuzzo, L.   (2023).   A Model of Ganymede's Magnetic and Plasma Environment During the Juno PJ34 Flyby.   *Journal of Geophysical Research: Space Physics*, *128*(12), e2023JA032113.   Retrieved from https://agupubs.onlinelibrary.wiley.com/doi/abs/10.1029/ 2023JA032113 (e2023JA032113 2023JA032113) doi: https://doi.org/10.1029/ 2023JA032113

Szabo, P. S., Poppe, A. R., Mutzke, A., Liuzzo, L., & Mogan, S. R. C.   (2024, feb).   Backscattering of Ions Impacting Ganymede's Surface as a Source for Energetic Neutral Atoms.   *The Astrophysical Journal Letters*, *963*(1), L32. Retrieved from https://dx.doi.org/10.3847/2041-8213/ad2701   doi: 10.3847/2041-8213/ad2701

Tawara, H., Kato, T., & Nakai, Y.   (1985).   Cross sections for electron capture and loss by positive ions in collisions with atomic and molecular hydrogen. *Atomic Data and Nuclear Data Tables*, *32*(2), 235-303.   Retrieved from https://www.sciencedirect.com/science/article/pii/0092640X85900075 doi: https://doi.org/10.1016/0092-640X(85)90007-5

Tippens, T., Liuzzo, L., & Simon, S. (2022). Influence of Titan's Variable Electro-

magnetic Environment on the Global Distribution of Energetic Neutral Atoms. *Journal of Geophysical Research: Space Physics*, *127*(10), e2022JA030722. Retrieved from `https://agupubs.onlinelibrary.wiley.com/doi/abs/10.1029/2022JA030722` (e2022JA030722 2022JA030722) doi: https://doi.org/10.1029/2022JA030722

Tippens, T., Roussos, E., Simon, S., & Liuzzo, L. (2024). A Novel Backtracing Model to Study the Emission of Energetic Neutral Atoms at Titan. *Journal of Geophysical Research: Space Physics*, *129*(1), e2023JA032083. Retrieved from `https://agupubs.onlinelibrary.wiley.com/doi/abs/10.1029/2023JA032083` (e2023JA032083 2023JA032083) doi: https://doi.org/10.1029/2023JA032083

Tippens, T., Simon, S., & Roussos, E. (2024). Modeling the Emission of Energetic Neutral Atoms in Titan's Dynamic Magnetospheric Environment. *Journal of Geophysical Research: Space Physics*, *129*(11), e2024JA033103. Retrieved from `https://agupubs.onlinelibrary.wiley.com/doi/abs/10.1029/2024JA033103` (e2024JA033103 2024JA033103) doi: https://doi.org/10.1029/2024JA033103

Tosi, F., Roatsch, T., Galli, A., Hauber, E., Lucchetti, A., Molyneux, P., . . . Lorente, R. (2024, August). Characterization of the Surfaces and Near-Surface Atmospheres of Ganymede, Europa and Callisto by JUICE. *Space Science Reviews*, *220*(5), 59. doi: 10.1007/s11214-024-01089-8

Turc, L., Leclercq, L., Leblanc, F., Modolo, R., & Chaufray, J.-Y. (2014). Modelling Ganymede's neutral environment: A 3D test-particle simulation. *Icarus*, *229*, 157-169. doi: https://doi.org/10.1016/j.icarus.2013.11.005

Valek, P. W., Waite, J. H., Allegrini, F., Ebert, R. W., Bagenal, F., Bolton, S. J., . . . Wilson, R. J. (2022). In Situ Ion Composition Observations of Ganymede's Outflowing Ionosphere. *Geophysical Research Letters*, *49*(24). doi: https://doi.org/10.1029/2022GL100281

Vance, S. D., Styczinski, M. J., Bills, B. G., Cochrane, C. J., Soderlund, K. M., Gómez-Pérez, N., & Paty, C. (2021). Magnetic Induction Responses of Jupiter's Ocean Moons Including Effects From Adiabatic Convection. *Journal of Geophysical Research: Planets*, *126*(2), e2020JE006418. Retrieved from `https://agupubs.onlinelibrary.wiley.com/doi/abs/10.1029/`

2020JE006418   (e2020JE006418 2020JE006418) doi: https://doi.org/10.1029/ 2020JE006418

Vogt, M. F., Bagenal, F., & Bolton, S. J.   (2022).   Magnetic Field Conditions Upstream of Ganymede.   *Journal of Geophysical Research: Space Physics*, *127*(12), e2022JA030497.   Retrieved from `https://agupubs.onlinelibrary` `.wiley.com/doi/abs/10.1029/2022JA030497`   (e2022JA030497 2022JA030497) doi: https://doi.org/10.1029/2022JA030497

Vorburger, A., Fatemi, S., Carberry Mogan, S. R., Galli, A., Liuzzo, L., Poppe, A. R., ... Wurz, P. (2024). 3D Monte-Carlo simulation of Ganymede's atmosphere.   *Icarus*, *409*, 115847.   Retrieved from `https://www.sciencedirect` `.com/science/article/pii/S0019103523004268`   doi: https://doi.org/ 10.1016/j.icarus.2023.115847

Vorburger, A., Fatemi, S., Galli, A., Liuzzo, L., Poppe, A. R., & Wurz, P.   (2022). 3D Monte-Carlo simulation of Ganymede's water exosphere.   *Icarus*, *375*, 114810. Retrieved from `https://www.sciencedirect.com/science/article/` `pii/S0019103521004565` doi: https://doi.org/10.1016/j.icarus.2021.114810

Vorburger, A., & Wurz, P.   (2018, march).   Europa's Ice-Related Atmosphere: The Sputter Contribution. *Icarus*, *311*, 135–145. doi: 10.1016/j.icarus.2018.03.022

Weber, T., Moore, K., Connerney, J., Espley, J., DiBraccio, G., & Romanelli, N.   (2022).   Updated Spherical Harmonic Magnetic Field Moments of Ganymede From the Juno Flyby.   *Geophysical Research Letters*, *49*(23).   doi: https://doi.org/10.1029/2022GL098633

Wedlund, C., Bodewits, Dennis, Alho, Markku, Hoekstra, Ronnie, Behar, Etienne, Gronoff, Guillaume, ... Beth, Arnaud   (2019).   Solar wind charge exchange in cometary atmospheres - I. Charge-changing and ionization cross sections for He and H particles in H2O.   *A&A*, *630*, A35.   Retrieved from `https://doi.org/10.1051/0004-6361/201834848`   doi: 10.1051/0004-6361/201834848

Williams, D. J. (2001). Ganymede's ionic radiation belts. *Geophysical Research Letters*, *28*(19), 3793–3796. doi: 10.1029/2001GL013353

Williams, D. J., Mauk, B., & McEntire, R. W.   (1997).   Trapped electrons in Ganymede's magnetic field.   *Geophysical Research Letters*, *24*(23), 2953–2956. doi: 10.1029/97GL03003

Williams, D. J., Mauk, B., & McEntire, R. W. (1998, 8). Properties of Ganymede's magnetosphere as revealed by energetic particle observations. *Journal of Geophysical Research: Space Physics*, *103*(A8), 17523–17534. doi: 10.1029/98JA01370

Zhan, X., & Schubert, G. (2012). Powering Ganymede's dynamo. *Journal of Geophysical Research: Planets*, *117*(E8). Retrieved from `https:// agupubs.onlinelibrary.wiley.com/doi/abs/10.1029/2012JE004052` doi: https://doi.org/10.1029/2012JE004052

Zhou, H., Tóth, G., Jia, X., & Chen, Y. (2020). Reconnection-Driven Dynamics at Ganymede's Upstream Magnetosphere: 3-D Global Hall MHD and MHD-EPIC Simulations. *Journal of Geophysical Research: Space Physics*, *125*(8), e2020JA028162. doi: https://doi.org/10.1029/2020JA028162